DFe patterns impacted by shallow hydrothermal sources along a transect through the Tonga-Kermadec arc

Chloé Tilliette[1], Vincent Taillandier[1], Pascale Bouruet-Aubertot[2], Nicolas Grima[3], Christophe Maes[4], Maryline Montanes[1], Geraldine Sarthou[5], Maria-Elena Vorrath[6], Veronica Arnone[7], Matthieu Bressac[8], David González-Santana[9], Frédéric GAZEAU[10], and Cécile Guieu[11]

[1]Sorbonne Université, CNRS, Laboratoire d'Océanographie de Villefranche
[2]Pierre and Marie Curie University
[3]French National Centre for Scientific Research (CNRS)
[4]LOPS/IRD
[5]Institut Universitaire Europeen de la mer
[6]Univ Hamburg, Inst Geol, Bundesstr 55, D-20146 Hamburg, Germany
[7]6Instituto de Oceanografía y Cambio Global, IOCAG, Universidad de Las Palmas de Gran Canaria
[8]French National Centre for Scientific Research
[9]Univ Brest, CNRS, IRD, Ifremer, LEMAR
[10]Unknown
[11]Laboratoire d'Oceanographie de Villefranche (LOV)

November 26, 2022

Abstract

In the Western Tropical South Pacific, a hotspot of N2-fixing organisms has recently been identified. The survival of these species depends on the availability of dissolved iron (dFe). dFe was measured along a transect from 175 °E to 166 °W near 19-21 °S. The distribution of dFe showed high spatial variability: low concentrations (~0.2 nmol kg-1) in the South Pacific gyre and high concentrations (up to 50 nmol kg-1) west of the Tonga arc, indicating that this arc is a clear boundary between iron-poor and iron-rich waters. An optimal multiparameter analysis was used to distinguish the relative importance of physical transport relative to non-conservative processes on the observed dFe distribution. This analysis demonstrated that distant sources of iron play a minor role in its distribution along the transect. The high concentrations observed were therefore attributed to shallow hydrothermal sources massively present along the Tonga-Kermadec arc. Nevertheless, in contrast to what has been observed for deep hydrothermal plumes, our results highlighted the rapid decrease in dFe concentrations near shallow hydrothermal sources. This is likely due to a shorter residence time of surface water masses combined with several biogeochemical processes at play (e.g., precipitation, photoreduction, scavenging, biological uptake). This study clearly highlights the role of shallow hydrothermal sources on the dFe cycle within the Tonga-Kermadec arc where a strong link to biological activity in surface waters can be assessed. It also emphasizes the need to consider the impact of these shallow hydrothermal sources for a better understanding of the global iron cycle.

DFe patterns impacted by shallow hydrothermal sources along a transect through the Tonga-Kermadec arc

C. Tilliette[1*], V. Taillandier[1], P. Bouruet-Aubertot[2], N. Grima[3], C. Maes[3], M. Montanes[1], G. Sarthou[4], M-E. Vorrath[5], V. Arnone[6], M. Bressac[1], D. González-Santana[4], F. Gazeau[1] and C. Guieu[1*]

[1]Sorbonne Université, CNRS, Laboratoire d'Océanographie de Villefranche, LOV, 06230, Villefranche-sur-Mer, France

[2]Sorbonne Université, CNRS, IRD, Laboratoire d'Océanographie et de Climatologie par Expérimentation et Approche Numérique (LOCEAN), Paris, France

[3]Univ Brest, CNRS, IRD, Ifremer, Laboratoire d'Océanographie Physique et Spatiale (LOPS, UMR 6523), IUEM, Brest, France

[4]Univ Brest, CNRS, IRD, Ifremer, LEMAR, F-29280 Plouzane, France

[5]Alfred Wegener Institute, Helmholtz Centre for Polar and Marine Research, 27568 Bremerhaven, Germany

[6]Instituto de Oceanografía y Cambio Global, IOCAG, Universidad de Las Palmas de Gran Canaria, ULPGC, 35017 Las Palmas de Gran Canaria, Spain

*Corresponding authors: Chloé Tilliette (chloe.tilliette@imev-mer.fr) and Cécile Guieu (cecile.guieu@imev-mer.fr)

Key Points:

- Shallow hydrothermal plumes of the Tonga-Kermadec arc are not transported over long distances, as previously reported for deep plumes.
- Surface scavenging and photoreduction of stabilizing-complexes mediate the low spatial dispersion of shallow hydrothermal dissolved iron.
- Nevertheless, the cumulative impact of multiple sources along the Tonga-Kermadec arc fertilizes the entire Lau Basin with dissolved iron.

Abstract

In the Western Tropical South Pacific, a hotspot of N_2-fixing organisms has recently been identified. The survival of these species depends on the availability of dissolved iron (dFe). dFe was measured along a transect from 175 °E to 166 °W near 19-21 °S. The distribution of dFe showed high spatial variability: low concentrations (~0.2 nmol kg^{-1}) in the South Pacific gyre and high concentrations (up to 50 nmol kg^{-1}) west of the Tonga arc, indicating that this arc is a clear boundary between iron-poor and iron-rich waters. An optimal multiparameter analysis was used to distinguish the relative importance of physical transport relative to non-conservative processes on the observed dFe distribution. This analysis demonstrated that distant sources of iron play a minor role in its distribution along the transect. The high concentrations observed were therefore attributed to shallow hydrothermal sources massively present along the Tonga-Kermadec arc. Nevertheless, in contrast to what has been observed for deep hydrothermal plumes, our results highlighted the rapid decrease in dFe concentrations near shallow hydrothermal sources. This is likely due to a shorter residence time of surface water masses combined with several biogeochemical processes at play (e.g., precipitation, photoreduction, scavenging, biological uptake). This study clearly highlights the role of shallow hydrothermal sources on the dFe cycle within the Tonga-Kermadec arc where a strong link to biological activity in surface waters can be assessed. It also emphasizes the need to consider the impact of these shallow hydrothermal sources for a better understanding of the global iron cycle.

1. Introduction

Iron (Fe) is the fourth most abundant element in the Earth's crust (about 6.7%; Rudnick & Gao, 2003) but it is present at sub-nanomolar concentrations in seawater (< 10^{-9} mol L^{-1}; Johnson et al., 1997). Yet, Fe is a key micronutrient for the growth and metabolism of all living organisms and especially phytoplankton for which it is essential for the proper functioning of the photosynthetic system (Behrenfeld & Milligan, 2013; Raven et al., 1999). Consequently, Fe has a direct influence on primary production (Martin et al., 1994; Sunda & Huntsman, 1995) and thus plays an important role on carbon export and sequestration in the ocean interior (Martin, 1990). Numerous natural fertilization studies have investigated the importance of iron, primarily in the Southern Ocean (Blain et al., 2007; Pollard et al., 2007), and have reported enhanced primary production rates and particulate organic carbon (POC) export efficiencies, which may

influence the biological carbon pump (Morris & Charette, 2013). In the context of climate change (IPCC, 2021), characterizing the elements governing the efficiency of this pump is of great interest. Due to its importance, the number of dissolved Fe (dFe) concentration measurements has increased impressively in recent years thanks to the GEOTRACES program (https://www.geotraces.org/), particularly in the deep ocean. However, there is still a lack of data for some key ocean regions, such as the Western Tropical South Pacific (WTSP) Ocean.

The WTSP Ocean (160 °E to 160 °W) has recently been identified as a hotspot of dinitrogen (N_2) fixation with some of the highest rates recorded in the global ocean (Bonnet et al., 2017). Diazotrophy is a process favored in phosphorus-rich, nitrogen-poor waters and fuels the ocean with novel nitrogen, helping to maintain ocean productivity and carbon sequestration (Caffin et al., 2018). This region is characterized by two biogeochemical subregions separated by the Tonga-Kermadec arc: (1) the South Pacific gyre located east of the arc and characterized by low N_2 fixation rates (~85 µmol N m^{-2} d^{-1}) despite sufficient phosphate availability (0.11 µmol L^{-1}; Moutin et al., 2008), and (2) the Melanesian archipelago together with the Lau Basin located west of the arc and characterized by high N_2 fixation rates (~631 µmol N m^{-2} d^{-1}; Bonnet et al., 2018). This spatial decoupling of N_2 fixation has been attributed to the alleviation of dFe limitation in the Melanesian archipelago (up to 60 nmol L^{-1} in the photic layer; Guieu et al., 2018) in contrast to the dFe-poor waters of the South Pacific gyre (Bonnet et al., 2008; Mills et al., 2004), with the Tonga-Kermadec arc acting as a frontier separating these two biogeochemical provinces.

The question of the iron origin in the WTSP Ocean remains however open. Multiple external sources of iron may be good candidates to explain iron availability in Melanesian waters (Tagliabue et al., 2017). These sources include potential sediment-derived iron inputs in the shallower waters of the arc, especially near the islands (Dutheil et al., 2018; Homoky et al., 2016; Raapoto et al., 2019). Similarly, the WTSP Ocean is surrounded by numerous ferromagnesian islands that may supply many terrigenous nutrients, including iron, through runoff from island slopes (Shiozaki et al., 2014). Other good candidates are atmospheric iron inputs emitted from the many aerial volcanoes hosted by the WTSP Ocean. However, these were quantified during the OUTPACE cruise (Moutin & Bonnet, 2015) and Guieu et al. (2018) stated that they were too low to explain the dFe concentrations measured in the region. Another possibility is that dFe may be supplied by water masses of remote origin entering this region

(Mahadevan, 2016), therefore the role of physical transport must be also considered. Finally, the hypothesis that dFe comes from hydrothermal sources was proposed by Guieu et al. (2018) as they are known to be major sources of iron (German et al., 2016). Such sources are documented at shallow depths in the region (Massoth et al., 2007) and can directly fuel the photic layer (0-150 m) with novel dFe. The latter two hypotheses appear to be the most compelling and will be explored in detail in this work.

To understand the sources and sinks affecting the dFe distribution in the WTSP Ocean, we first present the dFe concentrations measured along a 6100 km transect near ~20 °S (Guieu & Bonnet, 2019; Fig. 1a). We then introduce the theoretical distribution of dFe using a water mass analysis. The anomalies between theoretical and measured dFe concentrations are then discussed to highlight the potential hydrothermal origin of dFe in the Lau Basin. Finally, the different processes involved are discussed to explain the longitudinal evolution of dFe.

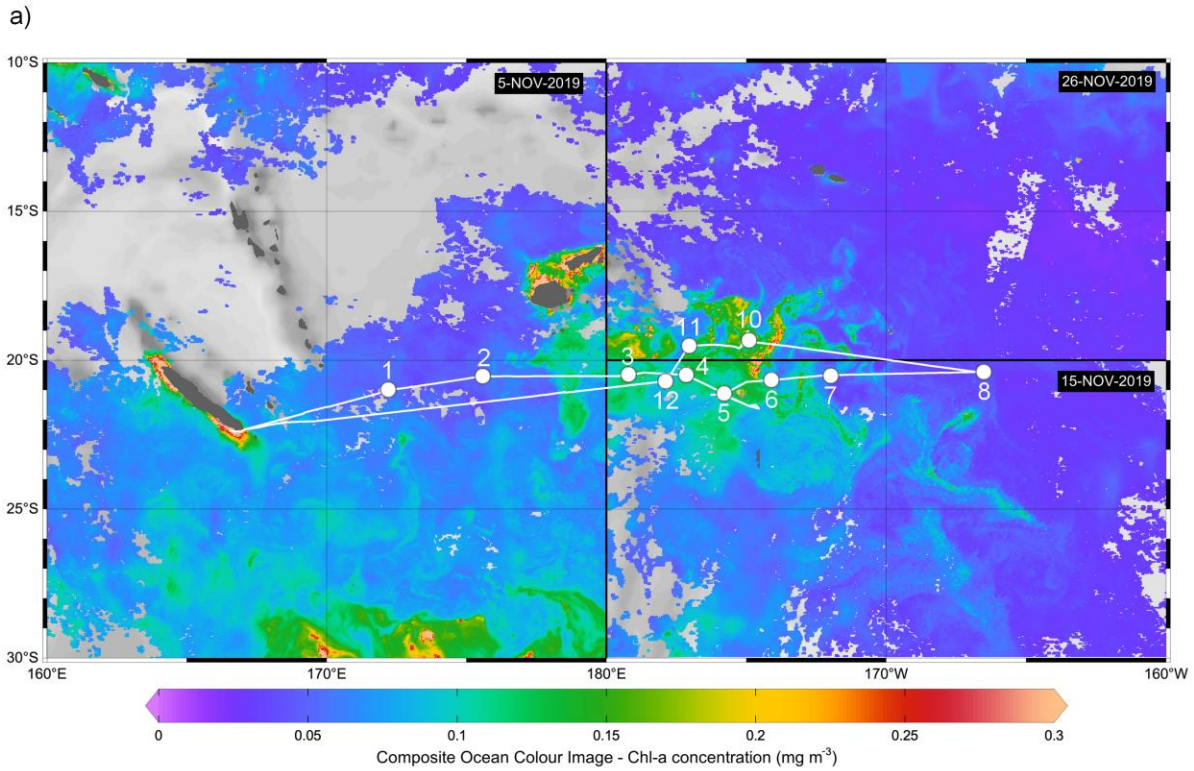
a)
5-NOV-2019
26-NOV-2019
15-NOV-2019
10°S
15°S
20°S
25°S
30°S
160°E
170°E
180°E
170°W
160°W
1
2
3
4
5
6
7
8
10
11
12
0
0.05
0.1
0.15
0.2
0.25
0.3
Composite Ocean Colour Image - Chl-a concentration (mg m-3)

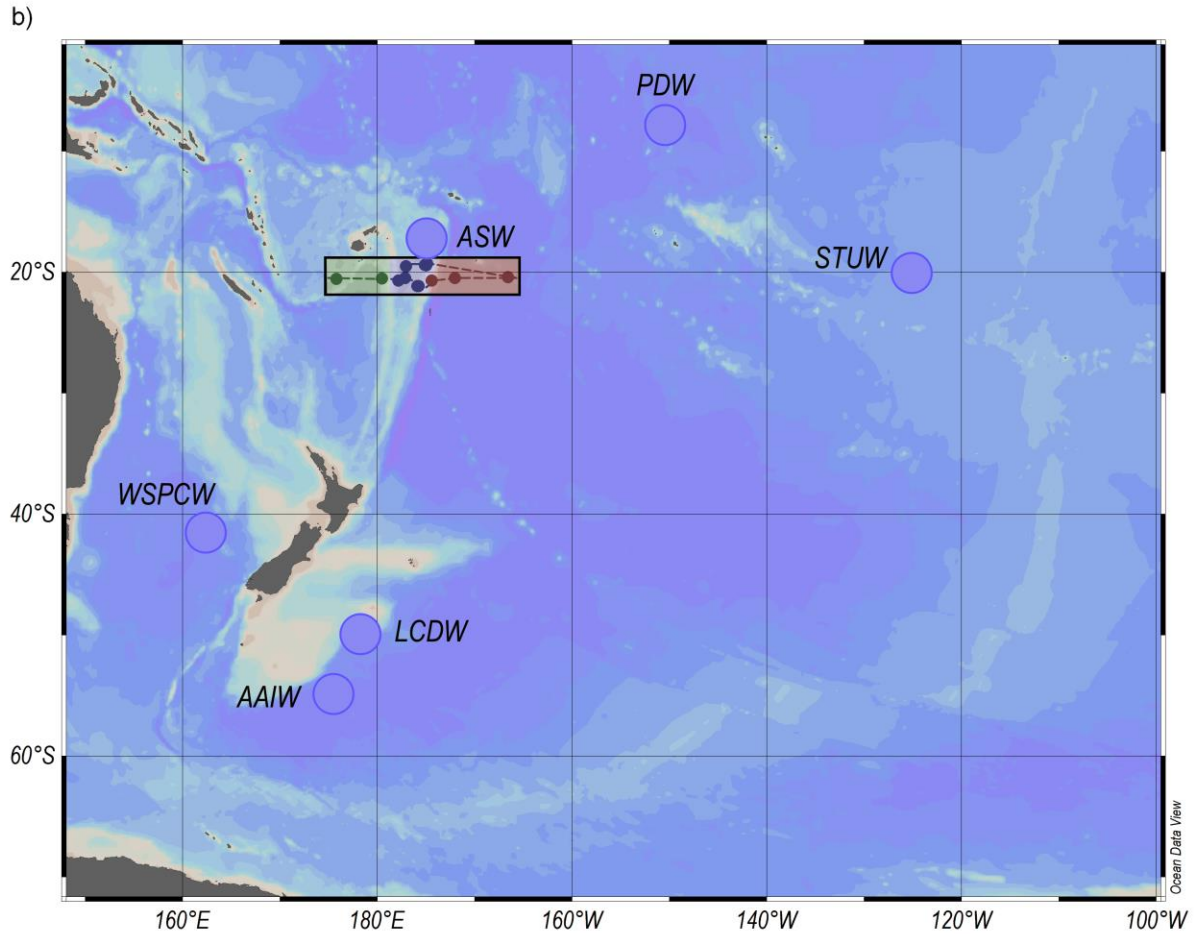
b)
PDW
ASW
STUW
WSPCW
LCDW
AAIW
20°S
40°S
60°S
160°E
180°E
160°W
140°W
120°W
100°W
Ocean Data View

Figure 1. **(a)** Transect of the cruise superimposed on surface chlorophyll-*a* concentrations (mg m^{-3}). Different oceanic regions were occupied during the cruise: Melanesian waters including short duration (SD) stations 1, 2 and 3, Lau Basin including SD 4, 11 and 12 as well as long duration (LD) stations 5 and 10, and the South Pacific gyre including SD 6, 7 and 8. Within each subregion are represented the chlorophyll-*a* concentrations observed over three time periods corresponding to the mean date of occupancy: 5 November 2019 for the western part of the transect, 15 November for the southeastern part and 29 November for the northeastern part. **(b)** Map of the South Pacific Ocean showing the transect of the cruise (small dots) and the location at which the end-members were defined (large blue dots). The frames around the transect represent the different subregions studied during the cruise: green for the Melanesian waters, blue for the Lau Basin and red for the South Pacific Gyre. See *Table 1* for end-members acronyms.

2. Materials and Methods

2.1. Oceanographic campaign presentation and sampling

The present study was conducted as part of the TONGA cruise (GPpr14; Guieu & Bonnet, 2019) that took place onboard the R/V L'Atalante from 31 October to 5 December 2019, along a transect extending from New Caledonia to the western end of the South Pacific gyre. This 6100 km-long transect allowed the characterization of the two biogeochemical zones of the region separated by the Tonga-Kermadec arc (Fig. 1). The objective of the cruise was to investigate the impact of shallow hydrothermal inputs on biogeochemical cycles, particularly trace metal cycles, downward export, and planktonic communities.

Investigated stations. Two types of stations were sampled: (a) nine short-duration stations (SD 1, 2, 3, 4, 6, 7, 8, 11 and 12) dedicated to biogeochemical sampling through water column vertical casts, (b) two long-duration stations (LD 5 and 10) dedicated to the impacts of hydrothermal fluids from two identified shallow sources along a short ~17 km transect including 5 substations, named from T5 to T1, with T5 being the closest to the hydrothermal source. For these two long-duration stations, the hydrothermal sources were identified through a precise dedicated bathymetric survey, using the one previously reported by Massoth et al. (2007), and the detection of acoustic anomalies on small caldera-like structures using a multibeam echosounder. The two T5 substations were positioned where the highest acoustic anomalies were recorded and the calderas of LD 5 and 10 were identified at 200 and 300 m, respectively. The T1 substations were then positioned as close as possible to T5 along the main current direction when the bottom was at ~2000 m for the deployment of a drifting mooring line left for five days. Between T1 and T5,

additional stations were staged to investigate the longitudinal impact of hydrothermal fluids released from T5. Following the eruption of New Late'iki (19.18 °S, 174.87 °W) one month prior to the cruise (a submarine volcano that turned into an island; Plank et al., 2020), an additional substation "Proxnov" near this site but located further north (15 km from LD 10-T5) was studied as part of LD 10.

CTD sampling. Temperature, conductivity (salinity), and dissolved oxygen vertical profiles were obtained using a rosette-mounted CTD SBE 9 plus sensor. At each station, (1) conventional CTD casts were conducted to sample inorganic nutrients using a rosette equipped with 24 Niskin bottles (12 L) and (2) Trace-Metal clean Rosette (TMR) casts were performed for dissolved and particulate trace metal sampling (see section 2.2). A total of 398 samples were collected for dFe analyses. Inorganic nutrients (nitrate: NO_3^-, phosphate: PO_4^{3-} and silicate: $Si(OH)_4$) were measured as detailed in Bonnet et al. (2018).

Autonomous platforms. Several autonomous instruments were deployed during the cruise at stations LD 5-T1 and T5, SD 11 and SD 12. Drifter observations were thus possible at the surface (0-15 m) through the deployment of Surface Velocity Program (SVP) drifters with the following WMO-id at the stations SD 12 (5501635, 5501636, 5501637, 5501638 and 5501639), LD 5-T1 (4101779, 4402504, 5102720, 5102721 and 6301680) and LD 5-T5 (5501630, 5501631, 5501632, 5501633 and 5501634; http://www.coriolis.eu.org/Data-Products/Data-Delivery/Data-selection) and at depth (1000-1500 m) through the deployment of deep Argo autonomous floats (https://fleetmonitoring.euro-argo.eu/dashboard) at the stations LD 5-T1 (6903025), LD 5-T5 (6902985), SD 11 (6902989) and SD 12: 6902927. The short trajectory (5 days, 0-1000 m) of the drifting mooring line deployed at LD 5-T1 could also be observed.

2.2. Dissolved iron measurements

All handling was performed under ultra-clean conditions (Bruland et al., 1979) following the guidelines established by the GEOTRACES cookbook (Cutter et al., 2017).

Preparation of the sampling material. All collecting material used was previously washed following a rigorous procedure. Nalgene® 60 mL low-density polyethylene (LDPE) bottles were first immersed in a surfactant bath (2% v/v, Decon™) for one week before being rinsed 3-times with MilliQ water (resistivity > 18.5 MΩ cm^{-1}). Bottles were then immersed in a Suprapure

hydrochloric acid solution (HCl, Supelco®; 10% v/v) for one month before being rinsed again 3-times with MilliQ water. Vials were finally one-third filled with 1% v/v Ultrapure HCl (Supelco®) and stored double-bagged pending use.

Sampling and storage of seawater samples. During the cruise, seawater samples were collected using GO-FLO bottles mounted on a TMR (General Oceanics Inc., Model 1018 Intelligent Rosette) attached to a 6 mm Kevlar line. Immediately after recovery, the rosette was transferred into a clean container for sampling. Bottles were pressurized with 0.2 µm-filtered nitrogen (Air Liquide®) allowing in-line filtration on 0.45 µm using acid-cleaned polyethersulfone filter (Supor®). Acid-cleaned bottles were rinsed 3-times with the sampled seawater before the final collection. Collected samples were acidified to pH 1.7 with Ultrapure HCl (0.2% v/v, Supelco®) within 24 h of collection and stored double-bagged pending analysis.

Dissolved iron analysis in seawater. Samples for dFe were analyzed in a clean room by flow injection and chemiluminescence detection (FIA-CL) at the Laboratoire d'Océanographie de Villefranche, as described by Blain et al. (2008) and adapted from the protocol originally described by Obata et al. (1997). Some improvements have been made compared to the last protocol. First, a new 8-hydroxyquinoline (8-HQ) resin was produced according to the protocol of Landing et al. (1986) where 8-HQ was immobilized on Fractogel TSK HW75-F (Tosoh Biosciences). The column was manufactured as described by Bowie et al. (1998) (i.e., the resin was placed in a rigid Teflon™ tube and isolated with clean quartz wool). Prior to each analysis day, two successive purifications of luminol on the 8-HQ resin were performed first on the pure luminol solution and then on the diluted solution. In addition, storage of the luminol solution in an opaque package significantly improved its shelf life and dosage reproducibility. Finally, the occasionally observed loss of sensitivity was resolved thanks to a 15-minute aqua regia flush performed every two analysis days to remove organics aggregated in the 8-HQ system that could not be eliminated by HCl alone.

Apart from these points, the method remained the same as in Blain et al. (2008). Briefly, the dosage was performed in a closed circuit, which implied no external manipulation and minimized contamination risk. All tubes used in the analytical system were made of Teflon™ except the Tygon™ tubes used for the peristaltic pump. Since 8-HQ selectively chelates dFe at pH 5, the pH of the samples was adjusted by adding Ultrapure ammonia (20-22%, Ultrex II, J.T.

Baker©) and a 3-times purified ammonium acetate buffer. Samples were then pre-concentrated on an 8-HQ chelating resin for 120 s. The chelated dFe was eluted with Suprapure HCl (0.7 M) and mixed with luminol (0.74 M), ammonia (1 M) and hydrogen peroxide (0.7 M). The luminescent reaction finally produced was detected by a photomultiplier at the end of the circuit. Given the wide range of measured dFe concentrations ([dFe]), the calibration curves were adapted to measure [dFe], up to 2 nM for most samples. The dFe-rich samples were diluted up to 1:20 depending on the concentration in a poor-dFe seawater collected at SD 8 also used as an in-house standard (dFe = 0.38 ± 0.03 nM, n = 26). The final concentration of those diluted samples did not exceed 5 nM and a 0-5 nM calibration curve was used in that case.

Validation of the measurements. Analytical blanks (i.e., reagent and manifold), calibration lines, and reference material values were determined each analysis day and are reported in Table S1. The mean analytical blank, calculated from the daily determinations with MilliQ water (n = 19), was 21 ± 22 pM and the detection limit (i.e., three times the standard deviation on the manifold blank divided by the calibration slope) was 16 ± 7 pM. Each sample was analyzed in triplicate. Method accuracy was evaluated daily by analyzing the GEOTRACES Surface (GS) seawater standard daily after each calibration and every 5-10 samples to validate measurements and monitor analytical stability. An in-house standard, whose concentration was previously determined by repeated analyses (n = 26) cross-calibrated with the GS standard, was also measured with the samples as an additional quality control. GS standard analyses for dFe averaged 0.510 ± 0.046 nM (n = 24) which compares well with community consensus concentrations of 0.546 ± 0.046 nM. It has to be noted that several replicates were measured to ensure the accuracy and reproducibility of the method and are reported in Table S1. All volumetric concentrations were converted to nmol kg^{-1} based on temperature and salinity data measured at each station and sampling depth.

2.3. Water mass analysis

An optimum multiparameter analysis (OMP) was used to resolve the water mass structure along the cruise transect (Tomczak, 1999). This method determines an optimal least-squares solution of a linear model of mixing equations to solve the contribution of selected water masses (i.e., end-members) as a function of a range of hydrologic parameters. In the equational system, the end-member contributions are used as variables and the hydrographic properties as parameters. In

this work, the available parameters are temperature (T), salinity (S), concentrations of dissolved oxygen (O_2), nitrate (NO_3^-), phosphate (PO_4^{3-}) and silicic acid ($SiOH_4$). However, the system is solved by assuming that all parameters are conservative (i.e., there is no sink or source in the ocean interior). This is not acceptable in our case as the selected end-members (see section 2.3.3) are distributed throughout the South Pacific where nutrients may be consumed through biological uptake and produced through organic matter remineralization and are, by definition, non-conservative. To account for these biogeochemical processes, an extended OMP (eOMP) was performed using the quasi-conservative parameters NO, PO and SiO for which remineralization or biological uptake have no effect (Broecker, 1974):

$$PO = [O_2] + R_{O_2/P} * [PO_4^{3-}] \quad (1)$$

$$NO = [O_2] + R_{O_2/N} * [NO_3^-] \quad (2)$$

$$SiO = [O_2] + R_{O_2/Si} * [Si(OH)_4] \quad (3)$$

where $R_{O_2/P}$, $R_{O_2/N}$ and $R_{O_2/Si}$ are the Redfield ratios that estimate the number of O_2 moles consumed for 1 mole of PO_4^{3-}, NO_3^- and $Si(OH)_4$ released during the process of organic matter remineralization, respectively. We assumed a $R_{O_2/P}$ = 155 (Anderson & Sarmiento, 1994), $R_{O_2/N}$ = 9.68 (Broecker, 1974; Peters et al., 2018) and $R_{O_2/Si}$ = 10.33 (Redfield et al., 1963). This led to the following constraint equations:

$$x_1T_1 + x_2T_2 + \ldots + x_nT_n = T_{sample} + \varepsilon_T \quad (4)$$

$$x_1S_1 + x_2S_2 + \ldots + x_nS_n = S_{sample} + \varepsilon_S \quad (5)$$

$$x_1PO_1 + x_2PO_2 + \ldots + x_nPO_n = PO_{sample} + \varepsilon_{PO} \quad (6)$$

$$x_1NO_1 + x_2NO_2 + \ldots + x_nNO_n = NO_{sample} + \varepsilon_{NO} \quad (7)$$

$$x_1SiO_1 + x_2SiO_2 + \ldots + x_nSiO_n = SiO_{sample} + \varepsilon_{SiO} \quad (8)$$

$$x_1 + x_2 + \ldots + x_n = 1 + \varepsilon_x \quad (9)$$

$$x_i \geq 0 \quad (10)$$

where x_n denotes the contribution of the *n*th end-member and ε refers to residual values that account for both measurement error and uncertainty in the assignment of end-member properties.

2.3.1. Overdetermined system

The eOMP must be realized as an overdetermined system, which means that the number of end-members must be strictly inferior to the number of parameters. We defined six end-members contributing to the cruise transect (see section 2.3.3) but only five parameters were available (T, S, NO, PO and SiO). The transect was therefore divided into two vertical domains in which the eOMP was performed independently, as it has been done in previous studies (e.g., Artigue et al., 2020; Fitzsimmons et al., 2016): (1) an upper domain comprising depths from 100 to 1000 m (density from 23.8 kg m^{-3} to 26.8 kg m^{-3}), and (2) a lower domain comprising depths from 1000 m to the seafloor (> 26.8 kg m^{-3}). The eOMP was performed using the OMP v2.0 MatLab package developed by Johannes Karstensen and Matthias Tomczak (https://omp.geomar.de/).

2.3.2. Upper layer inclusion

To consider depths including the shallow sources (0-200 m) in the analysis although the parameters could not be considered as conservative due to potential biological uptake, an artifactual water mass called Artifactual Surface Water (ASW) was created using salinity data obtained during the cruise at ~100 m. The limiting depth included in eOMP was selected when acceptable residuals were obtained (< 5%), leading to the exclusion of water masses above 100 m (< 23.8 kg m^{-3}). Since the excluded area is the area of maximum interest for surface communities, the inferred contributions and anomalies in the layers between 100 and 200 m are assumed not to be affected by biological processes.

2.3.3. End-member selection and data acquisition

End-member identification was performed based on hydrographic properties (potential density anomaly, salinity, oxygen and nitrate concentrations) observed along the transect profiles (Fig. S1) and the boundaries of each end-member zone were carefully defined by a thorough review of the literature. To present “pure” characteristics, end-members properties (Table 1) were selected from the core of the water masses from several databases (World Ocean Atlas, GLODAP and World Ocean Circulation Experiment) but were also found in the literature (Blain et al., 2008; Loscher et al., 1997; Tagliabue et al., 2012). End-members [dFe] were estimated using the GEOTRACES database. As the South Pacific is largely undersampled, especially for metals, only one data was available for the Antarctic Intermediate Water (AAIW). For quality purposes,

more data (n = 85) were found in the Antarctic Circumpolar Current where AAIW flows before reaching Tasmanian waters (Bostock et al., 2013) and resulted in a more accurate value for AAIW from 0.478 ± 0.000 nmol kg^{-1} (n = 1) to 0.426 ± 0.123 nmol kg^{-1} (n = 86).

Table 1. End-members characteristics (value ± uncertainty) used for the eOMP.

See the separate Excel file entitled "Table 1" or the table inserted at the end of the manuscript.

Acronym	Water mass name	T (°C)	S	$[O_2]$ (µmol kg^{-1})	$[PO_4^{3-}]$ (µmol kg^{-1})	$[NO_3^-]$ (µmol kg^{-1})	$[Si(OH)_4]$ (µmol kg^{-1})	"PO" (µmol kg^{-1})	"NO" (µmol kg^{-1})	"SiO" (µmol kg^{-1})	[dFe] (nmol kg^{-1})	Data source
ASW	Artifactual Surface Water	24.000 ± 0.750 *n=29*	34.450 ± 0.020 *n=29*	210.000 ± 8.700 *n=29*	0.100 ± 0.100 *n=12*	0.000 ± 0.610 *n=12*	1.000 ± 0.550 *n=13*	225.500 ± 24.200	210.000 ± 14.604	220.330 ± 14.381	0.180 ± 0.030 *n=9*	TONGA cruise, all stations, November 2019, 19-21 °S, 175 °E-165 °W, 100 m
STUW	Subtropical Underwater	24.464 ± 0.833 *n=27*	36.299 ± 0.136 *n=21*	208.535 ± 5.040 *n=28*	0.177 ± 0.030 *n=35*	0.117 ± 0.078 *n=21*	1.416 ± 0.260 *n=28*	235.984 ± 9.619	209.669 ± 5.797	223.171 ± 7.732	0.134 ± 0.018 *n=8*	World Ocean Atlas, World Ocean Circulation Experiment, Blain et al. (2008), 18-22 °S, 115-135 °W, 20-170 m
WSPCW	Western South Pacific Central Water	10.612 ± 0.994 *n=241*	34.886 ± 0.037 *n=248*	223.926 ± 12.560 *n=236*	0.915 ± 0.172 *n=233*	9.734 ± 4.113 *n=212*	5.839 ± 1.97 *n=232*	365.757 ± 39.215	318.15 ± 52.375	284.247 ± 32.959	0.440 ± 0.123 *n=19*	GEOTRACES GPY01, World Ocean Atlas, World Ocean Circulation Experiment, 39-43 °S, 155-175 °E, 250-500 m
AAIW	Antarctic Intermediate Water	4.317 ± 0.583 *n=96*	34.258 ± 0.037 *n=100*	232.836 ± 17.416 *n=73*	1.924 ± 0.143 *n=76*	28.533 ± 2.104 *n=65*	24.486 ± 6.538 *n=52*	531.076 ± 39.522	509.034 ± 37.78	485.786 ± 84.959	0.426 ± 0.123 *n=86*	GEOTRACES GPY01-06, World Ocean Atlas, World Ocean Circulation Experiment , 53-57 °S, 170 °E-180 °W, 500-1000 m
PDW	Pacific Deep Water	1.952 ± 0.142 *n=171*	34.662 ± 0.011 *n=170*	127.324 ± 11.914 *n=171*	2.713 ± 0.090 *n=171*	37.488 ± 0.977 *n=171*	140.151 ± 6.558 *n=171*	547.808 ± 25.801	490.206 ± 21.371	1575.087 ± 79.662	0.607 ± 0.072 *n=106*	GEOTRACES GP16, World Ocean Atlas, World Ocean Circulation Experiment, 7-11 °S, 160-140 °W, 2000-3000 m
LCDW	Lower Circumpolar Deep Water	0.914 ± 0.061 *n=116*	34.705 ± 0.003 *n=117*	209.459 ± 1.731 *n=108*	2.133 ± 0.062 *n=113*	32.118 ± 0.203 *n=114*	121.569 ± 1.885 *n=113*	540.061 ± 11.291	520.365 ± 3.700	1465.274 ± 14.381	0.635 ± 0.178 *n=8*	World Ocean Atlas, World Ocean Circulation Experiment, Loscher et al. (1997), Tagliabue et al. (2012), 48-52 °S, 172 °E-168 °W, 4000-5000 m

2.3.4. Parameters weighting

Parameters were weighted according to their signal-to-noise ratios (measurement accuracy) and conservative nature (conservative or quasi-conservative). The highest weight was set for T and S and mass conservation was assigned the same weight as the parameter with the highest weight (Tomczak & Large, 1989). In this study, different weights were tested for nutrients, ranging from values 12 to 4 times lower than T, S and mass conservation. Thereby, T, S and mass conservation were adjusted to 24 while nutrient weights were fixed to 4 as these weights led to the lowest residuals (Fig. S2).

2.4. Lagrangian particle tracking experiment

Lagrangian Particle Tracking Experiment (LPTE) was conducted to determine the main origin of the water masses crossing the cruise transect and thus to ensure the robustness and reliability of the defined end-member zones (Fig. 1b). The Ariane Lagrangian analysis software (http://www.univ-brest.fr/lpo/ariane) and a numerical dataset from a global ocean circulation model were used to perform this analysis. The dataset and LPTE method used in this study are described in the supporting information (see Text S1).

2.5. Statistical analyses

For [dFe], differences between stations as well as between different depth ranges were tested using a non-parametric Wilcoxon signed-rank test (wsrt), due to the non-independent and non-normally distributed samples. This test was performed using the R function "wilcox.test". Differences were considered significant at $p < 0.05$.

Iron anomalies along the transect were obtained by subtracting measured [dFe] during the cruise from theoretical [dFe] deduced from the eOMP. Permutation tests were performed to define a significance level above which the difference obtained actually represents an anomaly. The test used was the Monte-Carlo analysis and estimated the extent to which dFe anomalies could be affected by analytical errors of both FIA-CL and eOMP, as well as by the variability in end-members [dFe]. Thus, 1000 permutations of end-member dFe values were performed according to their standard deviation to estimate the propagated errors for each dFe anomaly. Since the highest error was ~0.2 nmol kg^{-1}, the anomaly threshold value was set at this value.

3. Results

3.1. Dissolved iron distribution in the WTSP Ocean

Sections of the [dFe] distribution are presented in Fig. 2, for the cruise transect (a) and for the small transects above the two shallow hydrothermal sources (b, c). Individual dFe vertical profiles are shown in Fig. 3 for SD (a, b, c) and LD (d, e, f) stations.

3.1.1. South Pacific gyre: east of the Tonga-Kermadec arc

The eastern part of the transect includes SD 6, 7, and 8 for which we can observe some differences in the dFe distribution. Stations furthest from the Tonga-Kermadec arc (i.e., SD 7 and 8) were characterized by low [dFe] in the upper layer (< 0.2 nmol kg^{-1}). Deeper, below 1000 m, a [dFe] enrichment was visible (0.5-0.6 nmol kg^{-1}) down to 3000 m for SD 7 and down to 4000 m for SD 8. The station closest to the arc (i.e., SD 6) was slightly different from the other stations of the gyre. Although [dFe] remain low throughout the whole water column (< 0.3-0.4 nmol kg^{-1}), [dFe] were higher than those at SD 7 and 8 (*wsrt*, p-value: 0.03), particularly in the first 100 m of the water column (*wsrt*, p-value: $5.28\ 10^{-6}$).

3.1.2. Melanesian waters: west of the Tonga-Kermadec arc

Melanesian waters constitute the westernmost part of the transect and include SD 2 and 3. This subregion was characterized by a dFe enrichment in the photic layer compared to the waters of the South Pacific gyre (*wsrt*, 0-200 m, p-value: 0.02) with [dFe] as high as 0.4-0.5 nmol kg^{-1}. Some peculiarities between the two stations were observable at depth. At SD 2, an increase in [dFe] above 0.5 nmol kg^{-1} was visible from 1000 m to the seafloor. An iron peak of ~0.8 nmol kg^{-1} centered at the same depth was also observed at SD 3, but this pattern decreases rapidly and [dFe] becomes constant at ~0.4 nmol kg^{-1} from 1200 m to the seafloor.

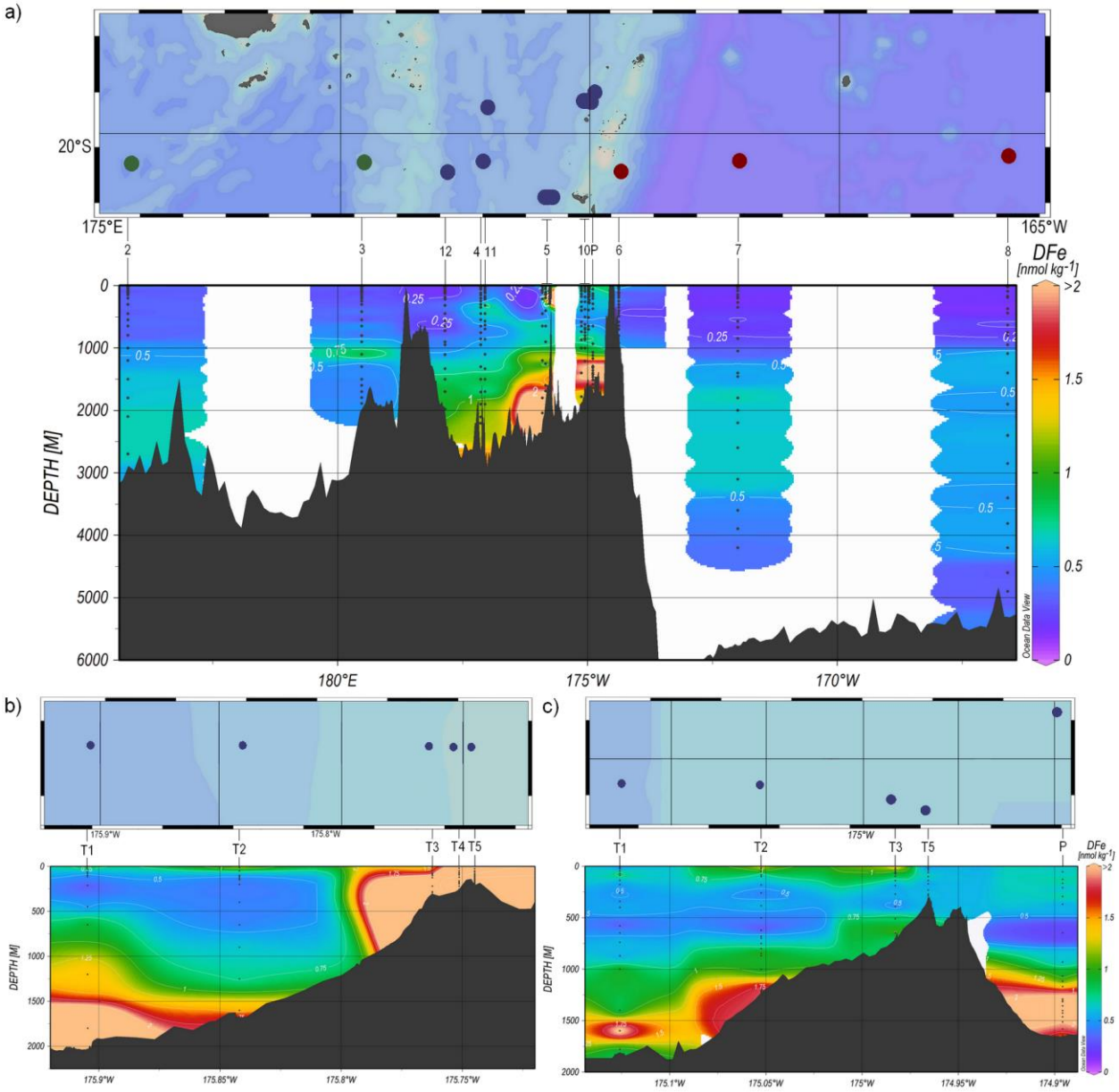

Figure 2. Sections of the dissolved iron (dFe) concentrations (nmol kg^{-1}) along the cruise transect **(a)** and along two smaller scale transects above LD 5 **(b)** and LD 10 **(c)**. The dots on the maps represent the position of the sampled stations and are colored according to the sub-region in which they are located: green for Melanesian waters, blue for the Lau Basin and red for the South Pacific gyre.

3.1.3. Lau Basin

SD stations. The Lau Basin, located between the Lau and Tonga ridges, is the central part of the transect and includes SD 4, 11, and 12 as well as LD 5 and 10 where two shallow hydrothermal sources were studied. In this oceanic basin, we observed higher [dFe] than in the South Pacific gyre (*wsrt*, p-value: 0.003) as well as in Melanesian waters (*wsrt*, p-value: 0.04) for all stations and over the entire water column. As for the other stations in the transect, some local differences were depicted for each profile. The westernmost station of the Lau Basin (i.e., SD 4) was characterized by [dFe] of 0.3-0.4 nmol kg^{-1} between 0 and 800 m. Below 800 m, an enrichment is observed with a maximum [dFe] of 1.2 nmol kg^{-1} at ~2200 m. SD 12 presented the least enriched photic layer, with [dFe] similar to those observed to the east (~0.2 nmol kg^{-1}, *wsrt*, p-value: 0.54). At depth, a gradual increase of [dFe] to ~1 nmol kg^{-1} was observed from 600 m to the seafloor. SD 11 had the highest [dFe] of the SD in the Lau Basin. In the photic layer, high [dFe] were observed (0.4-0.6 nmol kg^{-1}). As for SD 12, a gradual increase of [dFe] up to 1.6 nmol kg^{-1} was observed from 600 m to the seafloor. For both stations, a peak centered at ~320 m was visible, relatively low for SD 12 (0.4 nmol kg^{-1}) and rather high for SD 11 (1.6 nmol kg^{-1}).

LD 5. At LD 5, five substations were investigated: T5, located where the highest acoustic and chemical anomalies were found, and T4, T3, T2 and T1, which were located at 0.6, 2, 10 and 17 km from T5, respectively (Figs. 2b and 3d, e). At T5, high [dFe] (~50 nmol kg^{-1}) were observed 5 m above the seafloor (195 m), decreasing rapidly to ~18 nmol kg^{-1} at 185 m. These high [dFe] were maintained around 10-18 nmol kg^{-1} up to 100 m before decreasing in the photic layer to a [dFe] of ~1 nmol kg^{-1}. At T4, [dFe] were high in the photic layer, ranging from 0.4 to 2.9 nmol kg^{-1} and even higher at depth (~4-6 nmol kg^{-1}). Two [dFe] peaks were observed at 100 and 175 m. Shear profiles were observable at T3 from surface to bottom, with [dFe] fluctuating between 0.4 and 1.4 nmol kg^{-1} and a high [dFe] was visible just at the surface (0.8-1 nmol kg^{-1} at 0-50 m). The profiles of T1 and T2 were quite similar, characterized by high [dFe] in the first 100 m of the water column (0.5-2 nmol kg^{-1}). [dFe] remained constant at ~0.5 nmol kg^{-1} between 200 and 600 m before gradually increasing to the seafloor (2-2.5 nmol kg^{-1}).

LD 10. As for LD 5, four substations were surveyed at LD 10: T5, which was located on the edge of a small caldera summit, and T3, T2 and T1, which were 2, 8 and 15 km from T5. At T5, high [dFe] were observed in the entire profile (average ~0.6 nmol kg^{-1}). However, dFe enrichment was not as high as the one observed at LD 5-T5 (*wsrt*, p-value: 0.01). At T3, surface [dFe] were higher than just above the caldera summit, ranging from 2-3 nmol kg^{-1} between 0-35 m. Below 35 m, the profile remained constant at ~0.5 nmol kg^{-1}. At T2, [dFe] were still high between 0 and 80 m (0.5-1.5 nmol kg^{-1}). Below 80 m and down to 200 m, [dFe] decreased from 0.5 to 0.2 nmol kg^{-1}, followed by an increase to ~2 nmol kg^{-1} from 200 m to the seafloor. At T1, [dFe] were stable along the entire profile (~0.5 nmol kg^{-1}) except for two ~2 nmol kg^{-1} peaks observed at 100 and 1000 m. At Proxnov, [dFe] of ~0.7 nmol kg^{-1} were observable throughout the water column with maxima below 1000 m (2.5, 3.5 and 2 nmol kg^{-1} at 1250, 1400 and 1600 m, respectively).

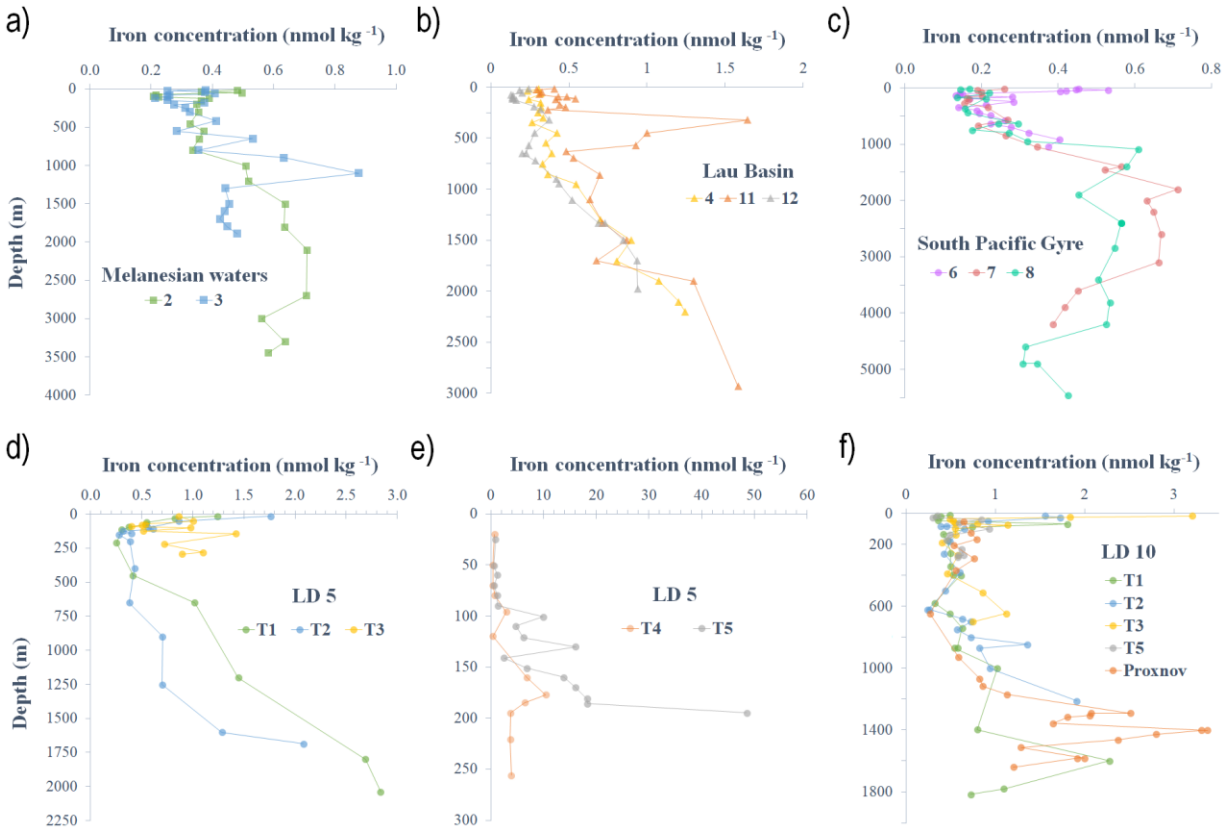

Figure 3. [dFe] profiles in Melanesian waters **(a)**, Lau Basin **(b)**, South Pacific gyre **(c),** in the different substations T5 to T1 of LD 5 **(d, e)** and LD 10 along with Proxnov **(f)**. [dFe] distribution at LD 5-T5 (i.e., the cast above the hydrothermal source) and LD 5-T4 are plotted separately **(e)** due to the high [dFe]. Note the different axis scales.

3.2. Water mass structure in the WTSP Ocean

3.2.1. Water mass definition

The surface layer (100 to 200 m) is characterized by constantly seasonally varying water properties due to ocean-atmosphere exchanges that have a significant impact on the temperature and salinity of the water mass (e.g., seasonal temperature variability, subtropical evaporation, and equatorial excess precipitation). This analytical issue was circumvented by creating the ASW, which is the only end-member contributing significantly to this layer. The main thermocline (200 to 700 m) includes the Subtropical Underwater (STUW) and the Western South Pacific Central Water (WSPCW). STUW originates from the subduction of high salinity waters from the equatorial part of the subtropical gyre and is associated with a shallow salinity maximum. Created by subduction and diapycnal mixing, WSPCW exhibits a linear temperature-salinity relationship over a wide range down to the intermediate layer. The intermediate layer (700 to 1300 m) was composed solely of AAIW, a low-salinity water mass originating from the sea surface at sub-Antarctic latitudes and characterized by a salinity minimum reached at 700 m. AAIW circulates around the subtropical gyre from the Southeastern Pacific, extending northwestward as tongues of low-salinity, high-oxygen water, and enters the tropics in the Western Pacific. The deep layer (> 1300 m) contains the Pacific Deep Water (PDW) and the Lower Circumpolar Deep Water (LCDW). PDW originates from the equatorial Pacific and flows southward. It is formed in the Pacific interior from the upwelling of the Antarctic Bottom Water (AABW). PDW is the oldest water in the global ocean, characterized by low oxygen, high nitrate contents and well-mixed temperature and salinity properties. LCDW originates from the Southern Ocean and overlaps the depth and density ranges of PDW. It can however be distinguished from PDW by a maximum of salinity and oxygen and a nitrate minimum. The property-property profiles of the dataset used for the eOMP and the properties of the defined end-members are shown in Fig. S3.

A posteriori, LPTE analyses were performed to ensure that the area chosen for the position and depth of each end-member agreed with the particle trajectories modeled in the region. The results of these analyses are shown in Figs. S4, S5 and S6. These analyses support the contribution of STUW to the thermocline layer of the cruise transect with particles following the South Pacific gyre circulation between 200-400 m, reaching the selected area for this water mass. Trajectories

are also in good agreement with the zone defined for WSPCW as particles, originating from the Southern Ocean, cross the Tasman Sea between 200 and 400 m before reaching the area of the cruise transect. LPTE trajectories were consistent with the current understanding of AAIW circulation: AAIW enters the Pacific Ocean from Eastern New Zealand between 700 and 1500 m and flows to the WTSP via several portions of water extending from the subtropical gyre, originating mainly from the Southeastern Pacific. The particle trajectories were also in agreement for PDW, as particles from the equatorial Pacific reach the PDW-defined zone at 1500-2500 m and flow towards the transect. Regarding LCDW, the LPTE analysis was consistent with the end-member area chosen for the eastern part of the transect, as particles from the Southern Ocean flow east of New Zealand before heading northwest and reaching the area of the transect. This analysis also corroborates the lack of LCDW contribution to the western part of the transect as demonstrated by the eOMP (see section 3.2.2) since no particles originating from this water mass reach the western part of the transect.

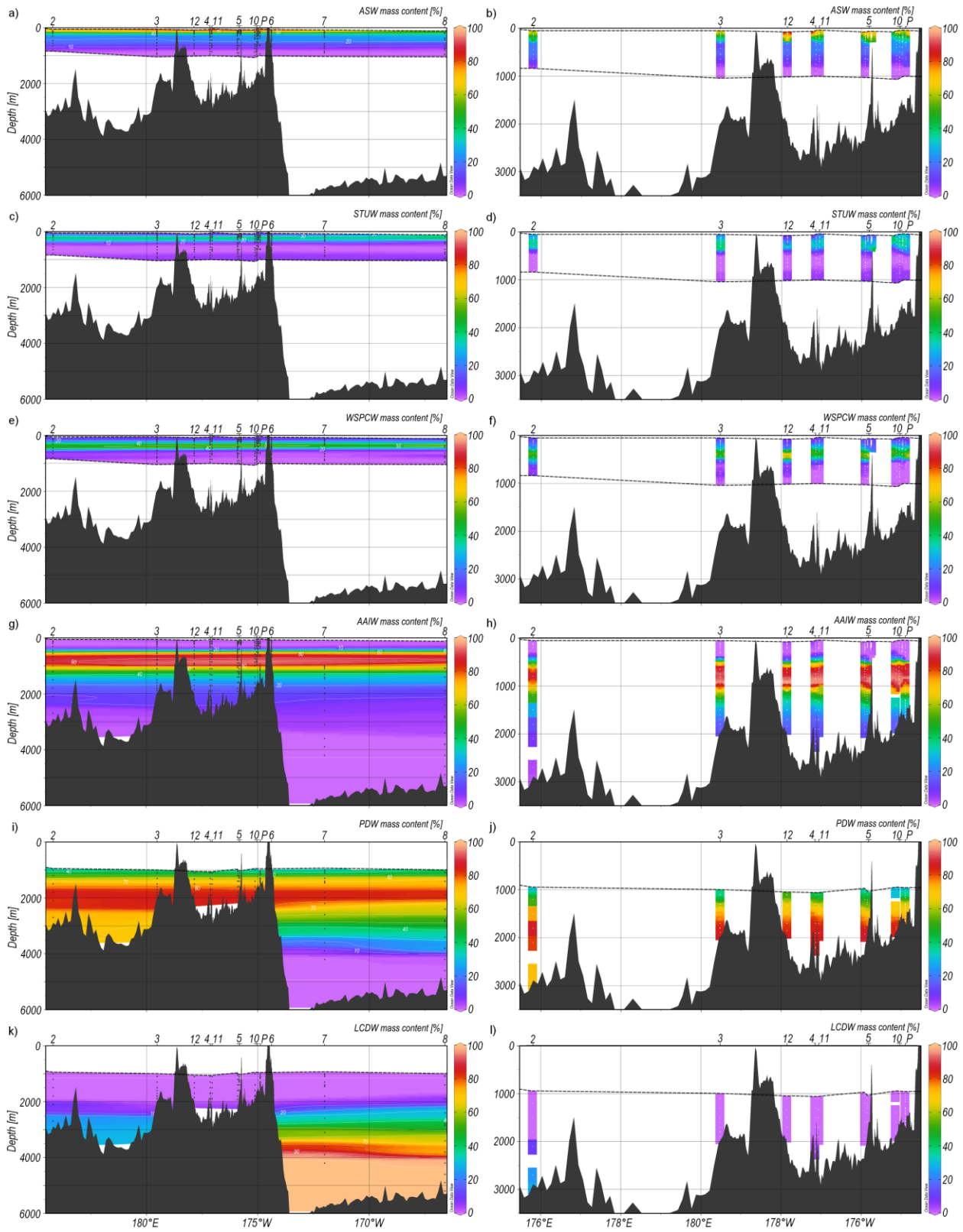

Figure 4. Contributions (%) of the different water masses to the cruise transect at each sampling depth according to the extended optimum multiparameter analysis (eOMP) for **(a)** the Artifactual Surface Water (ASW), **(c)** the

Subtropical Underwater (STUW), **(e)** the Western South Pacific Central Water (WSPCW), **(g)** the Antarctic Intermediate Water (AAIW), **(i)** the Pacific Deep Water (PDW) and **(j)** the Lower Circumpolar Deep Water (LCDW). The right panels represent the contributions of each water mass in the western part of the transect that includes Melanesian waters (SD 2 and 3) and Lau Basin (SD 4, 11 and 12; LD 5 and 10) with **(b)** ASW, **(d)** STUW, **(f)** WSPCW, **(h)** AAIW, **(j)** PDW and **(l)** LCDW. Sampling points are represented by black (left panel) and white (right panel) dots. The black dotted line represents the boundary above which the eOMP could not be applied (i.e., due to non-conservative parameters in the surface layer and residuals > 5%).

3.2.2. Vertical contribution of water masses along the cruise transect

The eOMP results allowed a detailed description of the contribution and distribution of the selected water masses (i.e., end-members) along the cruise transect (Fig. 4). A uniform zonal repartition of water masses was visible along the cruise transect, with the exception of the two deep end-members, PDW and LCDW, for which a different distribution for the eastern and western parts of the transect was observed. While PDW and LCDW contributed almost equally to the water masses in the eastern part of the transect below 1000 m, PDW was dominant in the western part (up to 90%). LCDW thus contributes to only 10-30% of the water masses in the western part of the transect, which contrasts with its high contribution (up to 100%) in the deepest waters of the South Pacific gyre.

According to the eOMP, the surface layer was mainly occupied by ASW with contributions greater than 60-90% in the 100-200 m depth range. This contribution decreased rapidly with depth to less than 30% at ~250 m and reaches zero contribution below 750 m. The thermocline layer was dominated by two water masses: STUW and WSPCW. STUW was present at depths between 100 and 450 m and reached its maximum contribution (> 40%) between 150 and 300 m. Below STUW, a layer of WSPCW was present along the transect with contributions exceeding 60% between 250 and 500 m. The maximum contribution of WSPCW was at ~400 m (60-70%). AAIW was present over a depth range of 450-1300 m and strongly dominated the intermediate layer with a contribution exceeding 90% between 700 and 1000 m. Its contribution decreased rapidly from 80% at 1000 m to 40% at 1300 m. The deep layer was occupied by two water masses that displayed differences in contribution for the western and eastern parts of the transect. Mixed with AAIW between 1000 and 1300 m, PDW occupied both intermediate and deep layers. It dominated the portion between 1300 and 2500 m with a contribution ranging from 60% to almost 100% in the eastern part of the transect. Its maximum contribution (60-90%) occupied a

larger depth range in the western part, as it reached the seafloor of the Melanesian waters (~3000 m) and Lau Basin (~4000 m). In contrast, the deeper seafloor of the South Pacific gyre (~6000 m) was not reached by PDW but by LCDW, a water mass present throughout the eastern section from 2000 m to the seafloor. Initially mixed with PDW until 3150 m (40%), its contribution increased to 60-70% between 3200 and 4000 m. LCDW then strongly dominated the deep layer below 4000 m with a contribution ranging from 90 to 100%. However, in the western part of the transect, LCDW was only present between 2500 m and the seafloor (~3000 m) in Melanesian waters and its contribution did not exceed 25%. Its contribution in the Lau Basin was negligible.

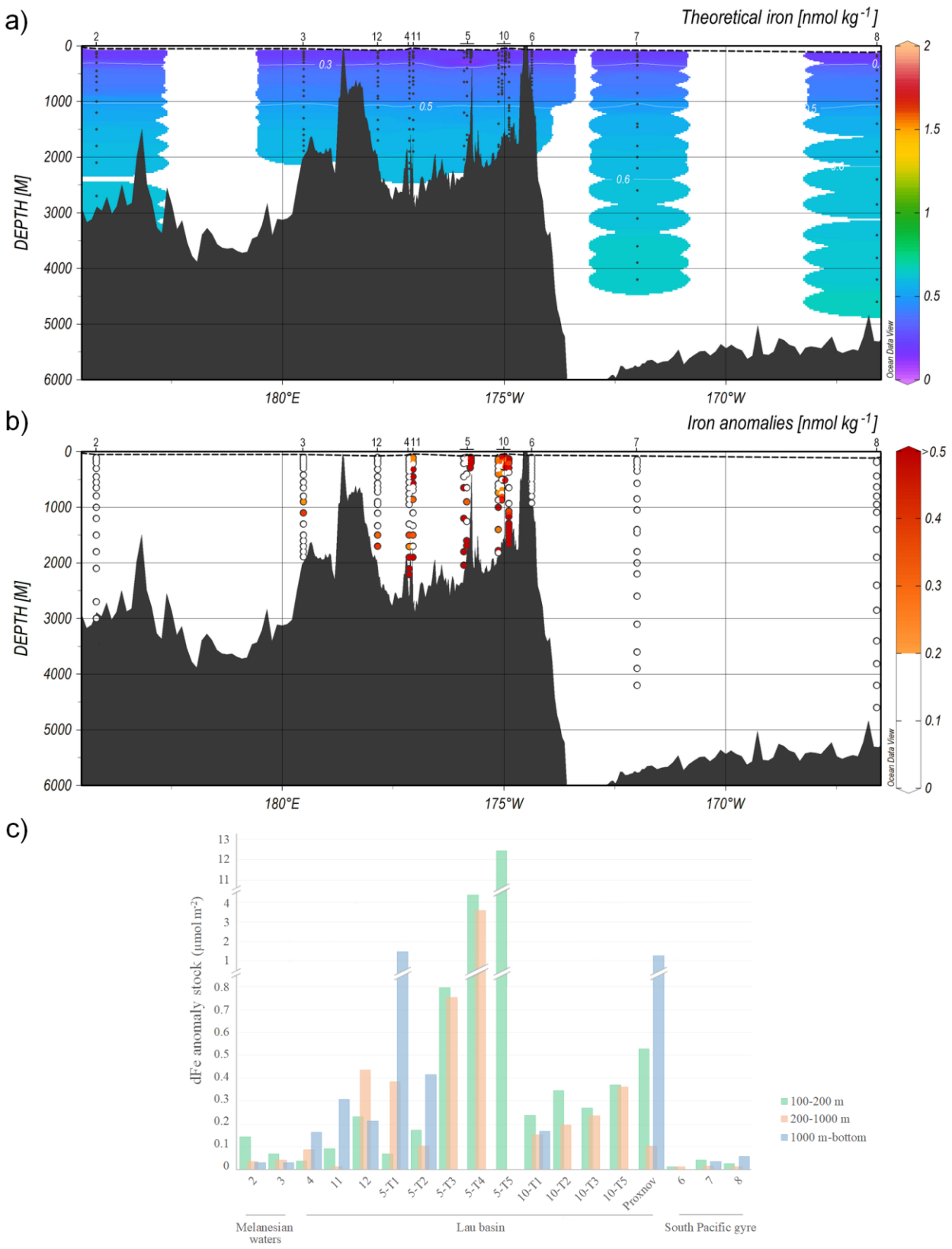
a)
Theoretical iron [nmol kg-1]
DEPTH [M]
180°E
175°W
170°W
Ocean Data View
b)
Iron anomalies [nmol kg-1]
DEPTH [M]
180°E
175°W
170°W
Ocean Data View
c)
dFe anomaly stock (µmol m-2)
100-200 m
200-1000 m
1000 m-bottom
2
3
4
11
12
5-T1
5-T2
5-T3
5-T4
5-T5
10-T1
10-T2
10-T3
10-T5
Proxnov
6
7
8
Melanesian waters
Lau basin
South Pacific gyre

Figure 5. **(a)** Theoretical dissolved iron (dFe) concentrations along the cruise transect obtained from the extended optimum multiparameter analysis (eOMP). **(b)** Iron anomalies representing the difference between measured and theoretical dFe concentrations. White dots correspond to iron anomaly values below the 0.2 nmol kg^{-1} significance threshold. **(c)** Histograms of the dFe anomaly stocks across the region integrated over the surface (100-200 m, green), intermediate (200-1000 m, orange) and deep layers (> 1000 m, blue). The order of appearance of the stations on the histogram is organized according to the geographic distribution of the sub-regions studied: the Melanesian waters (i.e., SD 2 and 3), the Lau Basin (i.e., SD 4, 11 and 12) also including LD 5 and 10 and finally the South Pacific gyre (i.e., SD 6, 7 and 8).

3.3. Iron anomalies along the WTSP Ocean

The eOMP-derived dFe transect represents the iron distribution resulting solely from water mass transport and physical mixing and acts as a control section without local sources. Those theoretical [dFe] were very low and homogeneous across the transect (Fig. 5a) depicting classic oceanic iron profiles for each station: low [dFe] in the upper layer (0.2-0.3 nmol kg^{-1}) and slightly higher [dFe] at depth (> 0.4 nmol kg^{-1}).

Iron anomalies presented in Fig. 5b were obtained by subtracting measured [dFe] (Fig. 2a) from theoretical [dFe]. The lowest anomalies (~0.09 nmol kg^{-1}) below the threshold value were observed for SD 6, 7 and 8. In the Melanesian waters, anomalies were higher but still below the threshold value, except for a few significant anomalies of ~0.3 nmol kg^{-1} observed at 1000 m for SD 3. Significant and large anomalies were found for stations located in the Lau Basin both at surface and at depth, except for SD 4 and 12 for which anomalies were only present below 1500 m.

DFe stocks attributed to local sources ("anomaly stocks") integrated over different layers are shown in Fig. 5c. No significant differences in anomaly stocks were observed between the three depth layers (100-200 m, 200-1000 m, 1000-bottom) for stations located east of the Tonga-Kermadec arc (SD 6, 7 and 8) and in Melanesian waters (SD 2 and 3). In contrast, some differences were observed in the Lau Basin depending on the depth layer considered, except for the westernmost SD 12. Large anomaly stocks were observable in all three layers at SD 12 (up to 0.4 µmol m^{-2}) but only in the deep layer for SD 4 (0.3 µmol m^{-2}). At LD 5, high anomaly stocks were visible in the photic layer from T5 to T3 (from 12.4 to 0.8 µmol m^{-2}) but decreased at T2 (0.17 µmol m^{-2}). In contrast, anomaly stocks in the deep and intermediate layers remained high for all LD 5 substations (0.4-3.6 µmol m^{-2}). At LD 10, large anomaly stocks were visible in the

surface layer at all substations although they were 10 times lower than at LD 5. At Proxnov, a large anomaly stock was visible in the photic and deep layers (0.5 and 1.1 µmol m^{-2}, respectively).

4. Discussion

4.1. Physical features of the study area

Physical processes at play in the region may provide insight into the distribution and fate of present observations of dFe. The large-scale circulation of the WTSP Ocean is well characterized (Reid, 1997) and is dominated by the anticyclonic South Pacific gyre. The South Equatorial Current (SEC) flows westward through the equatorial band and splits into several branches when it reaches the Lau Basin due to blocking of the SEC by islands associated with the Tonga and Lau arcs (Webb, 2000). In the western boundary, the SEC splits and joins the East Australian Current (EAC) that runs along the northwest coast of Australia before flowing eastward to feed the southern branch of the gyre. It then joins the Humboldt Current that flows northward along the continental coast of South America (Tomczak & Godfrey, 2003). Gyre waters then return to the equator through the SEC (Ganachaud et al., 2014). Thus, large-scale circulation patterns of the study area illustrate the presence of predominant westward currents associated with the SEC.

The eOMP coupled with a LPTE performed for this study allowed assessing the structure and mixing of water masses in the WTSP Ocean and estimates the theoretical distribution of dFe at the scale of our transect. As most geographic variation in water properties occurs in the meridional direction in the Pacific Ocean (Talley et al., 2007), it is not surprising that results showed a quasi-uniform zonal distribution of water masses in the transect conducted sufficiently far from the EAC along 20 °S. Due to bathymetry sills, deep water masses are not present in the Lau Basin, as its bowl-shaped seafloor prevents their entry. Thus, the westward-flowing subtropical gyre appears to collide with the bathymetric barrier represented by the Tonga-Kermadec arc.

Consequences of this bathymetric fracture could be discussed through observations of the surface and deep trajectories of autonomous instruments (SVP drifters and Argo floats, respectively) deployed during the cruise both in the center of the Lau Basin and along the Tonga-Kermadec

arc. In the center of the Lau Basin (> 100 km downstream of the arc), these trajectories showed the presence of a southwest flow regardless of the depth (Figs. S7a, c and S8a, c). Numerical simulations agree with these observations as Rousselet et al. (2018) showed a general transport west of 170 °W as follows: surface waters enter from the northeast via the SEC and propagate southwestward towards the various archipelagos present in the WTSP Ocean. Lagrangian velocities measured along the trajectories are about five times higher at the surface (SVP drifters: 0-15 m) than at depth (Argo floats: 1000-1500 m) in the Lau Basin. Now considering the Tonga-Kermadec arc (LD 5), Argo float trajectories (Figs. S8b, d) showed a southwestward flow at depth (1000 m). This observation is also supported by the southwestward trajectory of the drifting mooring (0-1000 m) deployed at the same site for five days (Fig. 6b). By contrast, at the surface, a large dispersion of the SVP drifters was observed. Their trajectories showed a turbulent surface flow (Figs. S7b, d) and the absence of a main stream, in agreement with Rousselet et al. (2018).

4.2. Dissolved iron distribution in the WTSP Ocean

This study has provided new insights into the oceanic iron cycle for several reasons. The Pacific Ocean is severely undersampled, especially for trace metals such as iron (Bruland & Lohan, 2006) and in the WTSP region for which very few data are available (Campbell et al., 2005; Cohen et al., 2021; Fitzsimmons et al., 2014; Guieu et al., 2018; Massoth et al., 2007). It yet represents a key region for understanding global dFe dynamics, particularly related to diazotroph activity. Furthermore, deep hydrothermal iron inputs are widely studied in all ocean regions in contrast to those induced by shallow hydrothermal vents associated with island arcs (Hawkes et al., 2014). The Tonga-Kermadec arc hosts a high density of submarine volcanoes associated with shallow hydrothermal sites (~2.6 vents/100 km; German et al., 2016; Massoth et al., 2007) and only Guieu et al. (2018) measured elevated [dFe] up to 60 nM in the photic layer and attributed them to shallow hydrothermal vents. For the first time, a dedicated survey of hydrothermal iron inputs has been conducted on shallow vents.

4.2.1 Iron sources: origin of the dissolved iron inputs

Our results demonstrated a low impact of physical dynamics and distant sources on dFe distribution along the transect. DFe distribution inferred from the eOMP shows low theoretical

[dFe] present throughout the transect, including in the Lau Basin. These theoretical [dFe], similar to open ocean iron data (Blain et al., 2008; Johnson et al., 1997), allow us to conclude that dFe originates, more probably, from local sources present in the WTSP region.

In the eastern part of the transect, the absence of dFe anomalies demonstrates that no local sources provide iron in the waters of the South Pacific gyre. However, it should be noted that a dFe enrichment of ~0.57 nmol kg^{-1} was measured between 1000 and 3000 m in the gyre (Fig. 2a; SD 7 and 8). It was initially considered as a deep distal plume from the East Pacific Rise (EPR), as Resing et al. (2015) measured a plume carrying rich [dFe] (~0.75 nmol kg^{-1} at 152 °W) thousands of km away from the source (located at 113 °W). Although this was a more northerly source, the EPR extends from North America to the tip of South America and hosts numerous vents that could have a similar impact on the entire ocean basin (Hudson et al., 1986; Menard, 1960). However, this hypothesis has been refuted by the eOMP, which demonstrates the absence of dFe anomalies to the east, although hydrothermal ^{3}He enrichment from the EPR (~30%) was measured at ~2500 m at 10-12 °S, 160-170 °W by Lupton et al. (2004). This suggests that the anomalies measured by Resing et al. (2015) ultimately merge with the [dFe] of the native deep water mass (0.61 ± 0.07 nmol kg^{-1}) and are no longer visible on this larger scale (~6000 km from the EPR) with this significance threshold. An absence of anomalies is also observed in Melanesian waters, except for two anomalies visible at 1000 m at SD 3, suggesting the absence of local sources in this subregion. It has to be noted that the iron-rich plume centered at ~180 °E as identified by Guieu et al. (2018) at the western border of the Lau arc in March 2015 was not sampled during our cruise. As hypothesized by the authors, the high [dFe] measured during this cruise could have been linked to a short-duration mega-plume related to an important submarine eruption event. The most notable dFe anomalies were found in the Lau Basin, particularly near the Tonga-Kermadec arc, where hydrothermal sources have already been reported (de Ronde et al., 2001; Massoth et al., 2007). Strong anomalies are visible both at surface and at depth, suggesting the presence of one or more local iron sources along this arc system.

As described previously, multiple iron sources exist in the open ocean (Tagliabue et al., 2017). Atmospheric iron inputs can be dismissed, as they were quantified by Guieu et al. (2018) as being at the lower end of reported values for the remote ocean and could not explain the large increase observed toward depth. In the WTSP region, four sources can potentially influence the distribution of dFe. Remineralization can impact the dFe distribution depending on the nature of

the particulate iron (pFe) present (Boyd et al., 2010; Bressac et al., 2019). This region is both a productive zone, rich in biogenic particles favoring remineralization, and a volcanic zone, rich in lithogenic particles enhancing scavenging. A balance between the two (i.e., source versus sink) could prevail in the region. However, remineralization has been quantified as redissolving only 1-2% of pFe (Boyd et al., 2010). In addition, Abadie et al. (2017) showed through an iron isotope study that remineralization occurs preferentially in intermediate waters, with particle desorption (John & Adkins, 2012; Labatut, 2014) being the primary source of dFe in deep waters. Thus, remineralization could not explain the dFe anomalies measured both at surface and at depth in the Lau Basin. Iron inputs from island origin could have a possible impact near the Melanesian archipelagos. This region hosts many ferromagnesian islands that could supply terrigenous nutrients, including iron, as hypothesized by Shiozaki et al. (2014), although these fluxes have not yet been quantified. Similarly, simulations from Dutheil et al. (2018) in the region showed that sediment-associated iron inputs near island margins could partly control *Trichodesmium* development. However, the latter two sources would primarily affect the coastal distribution of dFe at the WTSP Ocean scale and could not explain the observed patterns away from the islands. Model estimates (Tagliabue et al., 2010) and *in situ* measurements (Fitzsimmons et al., 2014, 2017; Resing et al., 2015) have shown a large-scale impact of deep hydrothermal-derived plumes on the dFe distribution, up to more than 4000 km off-axis. Such inputs could fertilize the entire Lau Basin and may explain the dFe anomaly patterns observed in this study. In this context, other sources seem negligible at the scale of the observed dFe enrichment, especially since it is remote from the islands.

Consistent with this hypothesis, literature and cruise data provide evidence for the hydrothermal origin of dFe in the WTSP Ocean for several reasons. This region has been reported to host numerous submarine volcanoes associated with a high density of hydrothermal fields (de Ronde et al., 2001; Massoth et al., 2007), and of these, two shallow hydrothermal sources were studied extensively during the cruise. LD 5-T5 appears to be the most active hydrothermal site. It displays typical chemical and acoustic features, including high turbidity associated with large amounts of particles, a suboxic environment with low pH (i.e., down to 6.3), low O_2 concentrations and high levels of H_2S, CH_4 and CO_2 (Dick et al., 2013). As reported in the literature in this area (Massoth et al., 2007) and elsewhere (e.g., Dick et al., 2013; González-Vega et al., 2020; Tarasov, 2006), significant amounts of dFe were released by this hydrothermal

site, especially since concentrations up to 50 nmol kg^{-1} were measured at 5 m above the seafloor. This shallow contribution appears to be higher than those from deep sources in the Pacific Ocean (10-17 nmol kg^{-1}; Fitzsimmons et al., 2014; Resing et al., 2015) but in the range of hydrothermal contributions measured in other oceanic regions (up to 57 nmol kg^{-1}; e.g., Conway & John, 2014). In addition, the highest dFe anomaly stock was recorded at the surface at this site and was 500 times higher than in the South Pacific gyre. Comparatively, LD 10-T5 seems to be a less active site, with a dFe anomaly stock in the photic layer 35 times lower than LD 5-T5 but still 15 times higher than in the gyre. Multiple clear acoustic anomalies were observed in the multibeam survey over this hydrothermal site during the cruise, indicating the presence of many weakly active sources. However, it should be noted that the dFe anomalies recorded at this site do not appear to be solely of hydrothermal origin, but could also be from the recent submarine eruption of New Late'iki one month before the cruise (i.e., October 13-23, 2019; Plank et al., 2020). This assumption seems reasonable since the New Late'iki eruption site, Proxnov and LD 10-T5 were only 10 and 15 km apart, respectively, and high dFe anomaly stocks were measured in the photic layer at Proxnov. A large anomaly stock was also estimated in the deep layer for this substation. Similarly, very abundant volcanic material was collected at 1000 m in sediment traps deployed at LD 10-T1 (Leblanc, pers. com. 2021) associated with the presence of a deep horizon of turbidity-identified particles. It can therefore be hypothesized that these large dFe anomalies and high particle abundance present throughout the water column originate from this submarine eruption. Thus, the hyperactive volcanism of New Late'iki may have pumped all the energy from the connected LD 10 system and explain the weakened sources relative to LD 5.

The strong dFe anomalies observed near the Tonga-Kermadec arc are thus not limited to the photic layer. Indeed, anomalies of the same order of magnitude have also been measured in the deep layer below 1000 m at LD 5-T1 and T2. This suggests the presence of many additional deep sources along the Tonga-Kermadec arc as reported in the literature (de Ronde et al., 2001; Massoth et al., 2007), some of them probably located near LD5-T1 where the highest anomaly stock was measured at depth. Such sources are known to release dFe-rich fluids, sometimes a million times enriched relative to ambient concentrations in the deep ocean (Von Damm, 1990) and the emitted plumes can be transported far from the source (Fitzsimmons et al., 2014, 2017; Resing et al., 2015).

4.2.2 Iron sinks: distribution and fate of dissolved iron

The question of the fate of dFe (i.e., stabilization versus loss) originating from deep and shallow hydrothermalism is also of great importance, particularly due to its influence on the biological carbon pump. Hydrothermal dFe was long thought to be lost near the source, but recent studies have shown that hydrothermal dFe from deep ocean ridges can be transported thousands of kilometers from the source (Fitzsimmons et al., 2014, 2017; Resing et al., 2015; Wu et al., 2011).

In agreement with these previous studies, our data show a wide dispersion of deep hydrothermal dFe over several hundred kilometers (~500 km). As mentioned in Section 4.2.1., deep sources appear to be active in the vicinity of the Tonga arc, around 1000 m near LD 5-T1. Thus, anomalies measured further west may be associated with the southwestward dispersion (see Section 4.1) of a deep plume from the arc. This deep iron-rich plume can be traced hundreds of kilometers from the source in the Lau Basin as well as in Melanesian waters, particularly at SD 3 where significant anomalies are visible at ~1000 m. The presence of such high concentrations far from the arc where hydrothermal sources have been identified (de Ronde et al., 2001; Massoth et al., 2007; Stoffers et al., 2006) is due to both advective transport and *in situ* geochemical conditions that allow dFe to remain in solution. The presence of strong iron-binding ligands may explain the stabilization of dFe at depth, especially since ligands have been reported to be abundant in hydrothermal plumes (Bennett et al., 2008; Sander & Koschinsky, 2011). Iron-ligand complexes (Fe-L) are known to enhance the solubility and stabilization of dFe (Boye et al., 2010; Gledhill, 2012; Hering & Morel, 1990; van den Berg, 1995) as they prevent the formation and adsorption of dFe into/onto particles and decrease the reactivity of Fe species (Bennett et al., 2008). Thus, the presence of ligands will mediate the interaction between pFe and dFe in favor of dFe. The formation of unreactive colloidal iron (cFe) could also regulate the stabilization of dFe as it prevents the dFe reactivity with other species or particles (Yücel et al., 2011). It should also be noted that the long residence time of water masses at depth (Fig. S8) should promote the accumulation of dFe near deep vents (Rijkenberg et al., 2018). All these processes could act together to regulate the stabilization of deep hydrothermal iron. However, to our knowledge, the processes governing the stabilization of shallow hydrothermal iron are less well known and should deserve more attention.

Compared to deep vents, a weak dispersion of shallow hydrothermal dFe in the WTSP region is suggested by our data. At LD 5, an almost instantaneous loss of dFe can be observed in the photic layer: 78% of the initial dFe supply (~50 nmol kg^{-1}) is lost over a distance of 600 m between T5 and T4 substations (~10 nmol kg^{-1}) and almost all dFe (97%) is lost over a distance of 16 km between T5 and T1 (~1 nmol kg^{-1}). At LD 10, 47% of the initial dFe input (~3.2 nmol kg^{-1}) is lost over a 7 km distance between T3 and T2 substations (~1.7 nmol kg^{-1}) and 85% of dFe is lost at T1 (~0.5 nmol kg^{-1}). Thus, in contrast to deep iron inputs (Bennett et al., 2008; Fitzsimmons et al., 2014, 2017; Resing et al., 2015), nearly all the dFe supplied by the shallow hydrothermal source appears to be lost over short distances. On a larger scale, away from the arc, surface dFe anomalies quickly become similar to those measured in Melanesian waters. Only 0.3 to 0.5 nmol kg^{-1} of dFe appears to be stabilized in the photic layer, representing 1 to 9% of the initial inputs of LD 5 and LD 10, respectively. An exception is observable for the northern SD 11 for which significant dFe anomalies were measured at surface, likely due to the additional impact from New Late'iki further north.

Thus, dFe from shallow hydrothermalism is less spatially spread than dFe from deep hydrothermalism. The oceanic iron cycle is affected by a series of processes that act together to set [dFe] in different parts of the ocean (Boyd et al., 2010). Some chemical processes influencing dFe removal can act in both shallow and deep environments (Johnson et al., 1997; Tagliabue et al., 2019). It is now widely accepted that most of dFe is rapidly precipitated near hydrothermal vents due to the rapid mixing of warm, H_2S-rich, O_2-poor, low pH fluids with cold, O_2-rich, high pH seawater (Beverskog & Puigdomenech, 1996; Lilley et al., 2013). This causes rapid precipitation of dFe into iron sulfides or rapid oxidation into iron oxyhydroxide precipitates, followed by settling on sediments near the source (Bruland & Lohan, 2006). Iron scavenging can also act in both layers and mediates the removal of dFe by surface adsorption onto sinking particles or by aggregation of cFe (Balistrieri et al., 1981; Goldberg, 1954; Turekian, 1977). This process is important in hydrothermal fields as vents release many lithogenic particles that can enhance the process near the source (Tagliabue & Resing, 2016). However, even though this process acts throughout the water column, scavenging is likely enhanced in the particle-rich surface layer as the residence time of dFe relative to scavenging has been reported to be faster in this layer (10 to 100 days; Black et al., 2020) than at depth (70 to 270 years; Bergquist & Boyle, 2006; Bruland et al., 1979). In addition, biological activities are likely to release high proportion

of biogenic particles and simulations from Beghoura et al. (2019) reported a lower sinking rate of small inorganic pFe compared to biogenic pFe (up to 2 orders of magnitude). Besides, some processes influencing dFe removal act exclusively in shallow environments. For example, biological uptake may influence the removal of shallow hydrothermal dFe. Similarly, the photochemical reactivity of dFe provides an additional sink relative to deep hydrothermalism. The UV portion of the solar spectrum plays a major role in the photoreduction of dFe (Rijkenberg et al., 2003), especially when bound to strong ligands. Light-induced reduction leads to dissociation of stable Fe-L complexes and unreactive colloids (Johnson et al., 1994; Miller et al., 1995). In turn, ligands undergo photo-oxidation and their photodegradation products have a lower conditional stability constant (Barbeau et al., 2003), similar to the weak iron-binding ligand classes (Rue & Bruland, 1995, 1997). This results in less stable iron species and thus ultimately to a dFe loss by scavenging. It should be noted that the short residence time of surface water masses (five times faster current velocity, Fig. S7) implies a low accumulation of dFe near the shallow source, in contrast to deep plumes.

With all these processes in mind and considering a steady state, we developed a simplified 1D 3-box budget to quantify the different processes that impact the hydrothermal dFe (Fig. 6a). This budget presents the evolution of [dFe] and the processes affecting its distribution vertically and horizontally over the small-scale LD 5 transect from T5 to T3. Quantification of each of the processes (precipitation, scavenging, photoreduction and biological uptake) was allowed by monitoring the evolution of [dFe] over the three substations following these equations:

$$P_{min}\ (\%) = 100 - \left(\frac{[dFe]_{max} * 100}{[dFe]_{input}}\right) \tag{11}$$

$$P_{max}\ (\%) = 100 - \left(\frac{[dFe]_{min} * 100}{[dFe]_{input}}\right) \tag{12}$$

where P represents one of the processes influencing the dFe distribution (precipitation, scavenging or photoreduction), with P_{min} and P_{max} referring to the minimum and maximum of the considered process. $[dFe]_{input}$ refers to the initial [dFe] of each sub-box. $[dFe]_{min}$ and $[dFe]_{max}$ are the minimum and maximum [dFe] resulting from the processes taking place in each sub-box.

For dFe biological uptake (BU), we considered the rates measured during the cruise (minimum uptake values (UR_{min}) = 9; maximum uptake value (UR_{max}) = 17 pmol kg^{-1} d^{-1}; Lory et al., 2022). The impact of biological uptake on [dFe] were estimated as follow:

$$BU_{min}\ (\%) = \left(\frac{UR_{min} * 100}{[dFe]_{input}}\right) \tag{13}$$

$$BU_{max}\ (\%) = \left(\frac{UR_{max} * 100}{[dFe]_{min}}\right) \tag{14}$$

where BU_{min} and BU_{max} are the minimum and maximum [dFe] removed by biological uptake.

At LD 5-T5, the water column is divided into three sub-boxes representing different layers in which distinct processes come into play: the (1) photic (0-90 m), (2) sub-photic (90-150 m) and (3) suboxic (150-200 m) layers. Sub-box (3) is characterized by high [H_2S] and decreasing pH and [O_2]. According to our budget, seawater conditions in this layer exclusively promoted the rapid precipitation (Lilley et al., 2013) of 86% of dFe into sulfides and/or oxyhydroxides. This estimate is in agreement with those reported in the literature for deep vents (32 to 90%; (Field & Sherrell, 2000; González-Santana et al., 2020; Lough et al., 2019). A vertical flux of 17 µmol dFe m^{-2} d^{-1} entering the sub-photic layer was estimated (see Text S2 for methodological details). Environmental conditions in the sub-photic layer no longer favor precipitation, due to stable pH and [O_2] and the absence of H_2S, and precipitation was considered negligible. In this layer, scavenging removed 9-63% of dFe. Since this wide range obtained by monitoring the disappearance of dFe was unsatisfying for our budget, this scavenging estimate was finally refined for the sub-box (2) by monitoring the appearance of pFe (see Text S3 for methodology of pFe measurements) according to the following equations:

$$S_{min}\ (\%) = 100 - \left(\frac{[pFe]_{input} * 100}{[pFe]_{min}}\right) \tag{15}$$

$$S_{max}\ (\%) = 100 - \left(\frac{[pFe]_{input} * 100}{[pFe]_{max}}\right) \tag{16}$$

where S_{min} and S_{max} refer to the minimum and maximum of scavenging. $[pFe]_{input}$ being the initial [pFe] of each sub-box. $[pFe]_{min}$ and $[pFe]_{max}$ are the minimum and maximum [pFe] resulting from the scavenging effect.

Obtained scavenging percentages were consistent with those estimated with dFe only, although narrower: 40-72% and 67-68% in sub-boxes (1) and (2), respectively, and of the same order of magnitude in the two layers. Those scavenging estimates are in good agreement, although slightly higher, with those reported in the literature (~50%; Forsgren et al., 1996; González-Santana et al., 2021). Vertical dFe fluxes into the photic layer from the sub-photic layer were one order of magnitude lower (1.9 µmol dFe m^{-2} d^{-1}) compared to fluxes from suboxic to sub-photic layers but still high enough to allow a significant vertical transport of dFe. In that layer, photoreduction, biological uptake and scavenging have to be considered. DFe consumption by surface phytoplankton has been reported to be low in the WTSP region, including above shallow hydrothermal sources (9-17 pmol L^{-1} d^{-1}; Lory et al., 2022). This uptake rate is similar to that reported in the literature (29 ± 19 pmol L^{-1} d^{-1}; Maldonado et al., 2005; Sunda & Huntsman, 1995) and accounts for only 0.7-3% of dFe removal. Assuming a similar scavenging rate in the photic and sub-photic layers, it was possible to estimate a photoreduction of 22-36% of dFe, in agreement with values previously reported in the literature (25 ± 21%; Kuma et al., 1992).

The second box refers to the LD 5-T4 substation and has been divided into two sub-boxes to discriminate processes acting exclusively in the photic layer. Since precipitation is assumed to be negligible far from the hydrothermal source due to seawater chemical conditions, scavenging is the main process acting in the sub-photic layer and was estimated to remove 35-72% of dFe. Biological uptake and photoreduction processes acting in the photic layer were estimated as described above, leading to a removal of dFe of 1-4% and 13-29%, respectively. The third box, divided into two sub-boxes, corresponds to LD 5-T3. Scavenging was estimated to remove 31-72% in the sub-photic layer while biological uptake and photoreduction were removing 1-4.3% and 14-24%, respectively, in the photic layer. It can be noted that the horizontal fluxes of dFe from T5 towards T4 and T3 could not be quantified due to a lack of accurate characterization of the vertical flow. Qualitatively, however, the horizontal flux would be diffusive in the photic layer and below, controlled by southwestward advection (as inferred from Lagrangian observations, see Section 4.1).

This budget indicates that the considered processes appear to act in similar proportion at all substations. In the photic layer, biological uptake is a negligible process in such iron-rich environment whereas photoreduction significantly impacts dFe distribution (removing up to 36% of dFe). In addition, scavenging also plays an important role in decreasing [dFe] in both layers as

it removes more dFe from solution (up to 72%) compared with data reported for deep sources (Forsgren et al., 1996; González-Santana et al., 2020).

It can be noted that T2 and T1 substations have been excluded from the budget because no significant [dFe] anomalies were found at these two substations. An impact of hydrothermal dFe from T5 was unlikely at these substations as the main stream at depth transported the plume southwestward (see Fig. 6b and Section 4.1). Nevertheless, the relatively large [dFe] (> 0.5 nmol kg^{-1}) observed at these substations could be due to the influence of other active shallow sources further north of the arc (Massoth et al., 2007).

DFe from shallow hydrothermal sources thus appears to be less spatially spread than dFe from deep sources due to the action of several processes (Johnson et al., 1997; Tagliabue et al., 2019). An influence of physical processes cannot be denied given the residence time of water masses, much shorter at the surface than at depth. The accumulation of dFe released by shallow hydrothermal sources will therefore be much lower than from sources located at depth. Biological processes do not have a significant impact on the distribution and fate of shallow hydrothermal dFe since our results showed a negligible effect of this process. Chemical processes appear to be the most important in mediating the fate of hydrothermal dFe in the photic layer. Although some of these, such as precipitation and scavenging, act throughout the water column, scavenging seems to act most effectively in the particle-rich surface layer. In addition, one mechanism for stabilizing dFe from deep plumes is complexation with ligands. However, photoreduction occurring in the photic layer implies a dissociation of dFe-stabilizing complexes, releasing inorganic dFe that can be rapidly removed from the dissolved pool. All these processes, not occurring in the deep dark ocean or to a lesser extent, act together to remove shallow hydrothermal dFe on a relatively small spatial scale (i.e., a few kilometers). Nevertheless, the cumulative impact of other active shallow sources identified in the vicinity of the Tonga-Kermadec arc (Fig. 6a) should fertilize the entire Lau Basin with dFe.

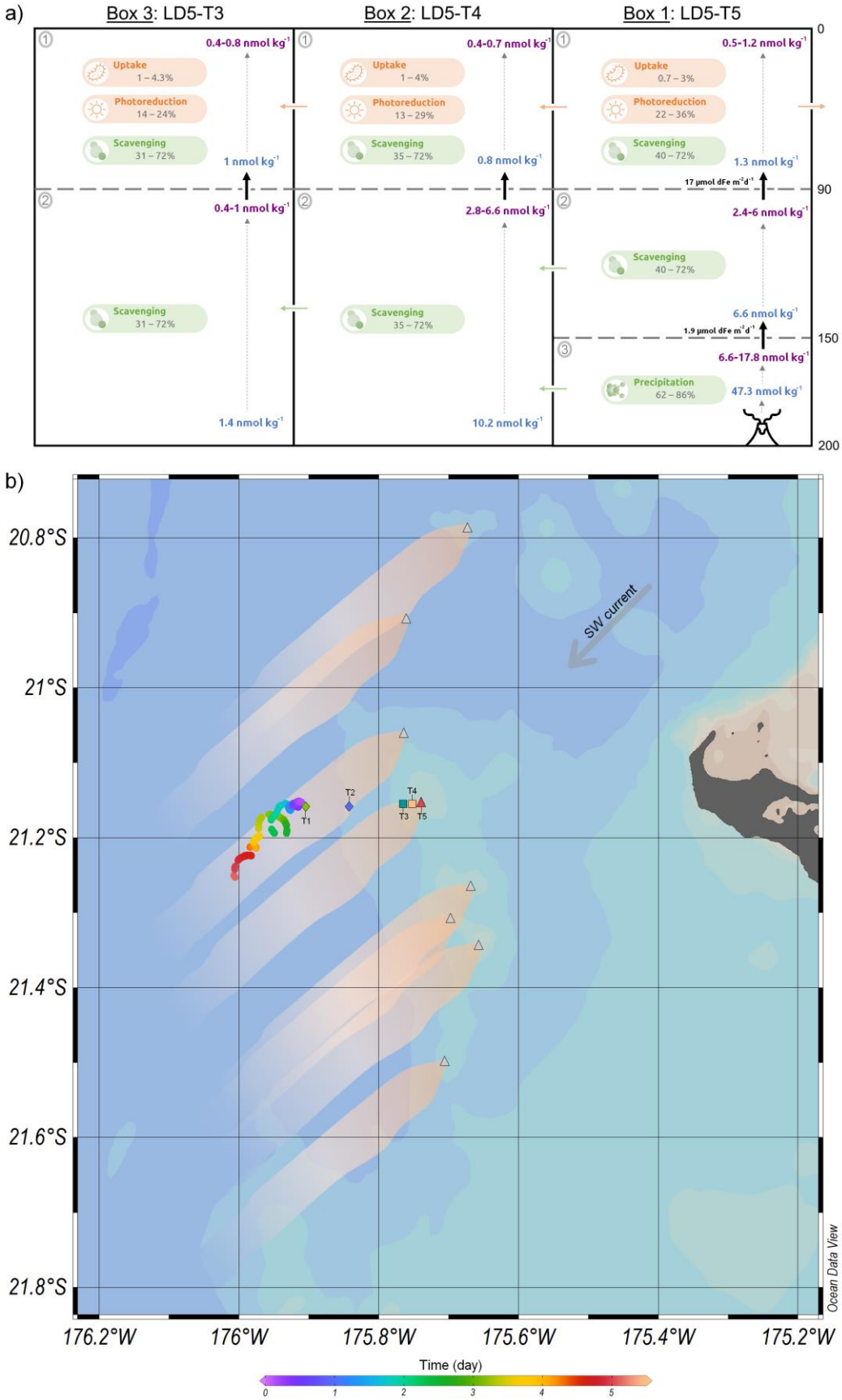
a)
Box 3: LD5-T3
Box 2: LD5-T4
Box 1: LD5-T5
0.4-0.8 nmol kg-1
Uptake 1 – 4.3%
Photoreduction 14 – 24%
Scavenging 31 – 72%
1 nmol kg-1
0.4-1 nmol kg-1
Scavenging 31 – 72%
1.4 nmol kg-1
0.4-0.7 nmol kg-1
Uptake 1 – 4%
Photoreduction 13 – 29%
Scavenging 35 – 72%
0.8 nmol kg-1
2.8-6.6 nmol kg-1
Scavenging 35 – 72%
10.2 nmol kg-1
0.5-1.2 nmol kg-1
Uptake 0.7 – 3%
Photoreduction 22 – 36%
Scavenging 40 – 72%
1.3 nmol kg-1
17 µmol dFe m-2d-1
2.4-6 nmol kg-1
Scavenging 40 – 72%
6.6 nmol kg-1
1.9 µmol dFe m-2d-1
6.6-17.8 nmol kg-1
Precipitation 62 – 86%
47.3 nmol kg-1
0
90
150
200
b)
20.8°S
21°S
21.2°S
21.4°S
21.6°S
21.8°S
SW current
T1
T2
T3
T4
T5
Ocean Data View
176.2°W
176°W
175.8°W
175.6°W
175.4°W
175.2°W
Time (day)
0
1
2
3
4
5

Figure 6. **(a)** Representation of the simplified 1D 3-box budget for substations T5, T4 and T3 of LD 5. The grey circled numbers in each box correspond to the number of the sub-boxes representing the (1) photic, (2) sub-photic and (3) suboxic layers. To the right is the depth considered for each sub-box in the budget. [dFe] used for the budget, namely the dFe input entering in each sub-box (i.e., either by the action of the hydrothermal source (sub-box (3)) or by physical processes) and the ranges (i.e., min-max) of [dFe] evolving in each sub-box from the initial input are represented in blue and purple, respectively. Orange cells represent processes acting exclusively in the photic layer while green cells represent processes that act in all layers. The non-dotted arrows represent transport: black for vertical diffusion, green for advective transport and orange for horizontal diffusion occurring only in the photic layer. **(b)** Conceptual diagram representing the dispersion of the measured plume at substations T5, T4 and T3 of LD 5 and the additional impact of plumes from sources further north or south of our Tonga arc study area on the Lau Basin. The colored points represent the southwestward trajectory of the drifting mooring (average flow on 0-1000 m) deployed at LD 5-T1 and left drifting for five days.

5 Conclusion

The Western Tropical South Pacific Ocean is characterized by the existence of a biogeochemical boundary between its western part, including the Lau Basin and Melanesian waters and characterized by high N_2 fixation, and its eastern part, comprising the western end of the South Pacific gyre and characterized by extremely low diazotrophy rates. Measurements of dFe concentrations in these two subregions confirm that this spatial decoupling of diazotrophy patterns can be explained by the attenuation of Fe limitation west of the Tonga-Kermadec arc. The question of the dFe origin was resolved using the results of an eOMP performed on the cruise transect. By separating the “conservative” component from the dFe section, it was possible to estimate the dFe component coming only from local sources, mostly from hydrothermal sources present in this region. Thus, this study was able to highlight the impact of shallow hydrothermal sources located along the Tonga-Kermadec arc on the dFe cycle of the WTSP Ocean. These sources release a large amount of dFe directly into the photic layer and can fertilize the entire Lau Basin and, to a lesser extent, the Melanesian zone. Such fertilization has a non-negligible impact on biological communities, particularly on diazotrophs such as *Trichodesmium* that are known to be widespread in this part of the Pacific Ocean. However, while dFe-rich plumes from deep sources appear to be stabilized and transported in Melanesian waters, dFe from shallow sources persists for only a few tens of kilometers. DFe is indeed lost very rapidly from solution by several physical, chemical, and biological processes such as precipitation and scavenging, some of them acting exclusively in the photic layer such as

photoreduction and, to a lesser extent, biological uptake. This weak stabilization of shallow hydrothermal dFe results in part from the dissociation of dFe-stabilizing complexes and weak dFe accumulation mediated by the faster ocean circulation in surface than at depth. Scavenging has also been reported to be more intense in the surface layer, accelerating the removal of shallow hydrothermal iron. Thus, dFe from shallow hydrothermal plumes of the Tonga-Kermadec arc does not appear to be transported over very long distances as previously demonstrated for deep hydrothermal plumes by many studies. Further analysis of the geochemical differences that may exist between shallow and deep hydrothermal sources and their environment is needed to better understand the stabilization of dFe and other metals in this region. For example, a thorough study of the various ligands released from shallow and deep hydrothermal sources in the region and an assessment of their stability is needed to understand the differences between these two types of hydrothermal systems. An investigation of the behavior of other trace metals released from such sources could help determine whether the low Fe dispersion observed in shallow hydrothermal environments is a distinct feature of that element or may be observed for other dissolved metals. In addition, further sampling of the Lau Basin with finer temporal and/or spatial scales may be necessary for a more thorough study of the dispersion of iron-rich shallow hydrothermal plumes.

Acknowledgments and Data

The entire dataset used in this study is currently available in the LEFE-CYBER database of the TONGA cruise (http://www.obs-vlfr.fr/proof/php/TONGA/tonga.php).

This work was performed in the framework of the TONGA project (dx.doi.org/10.17600/18000884) managed by the LOV (C. Guieu) and the MIO (S. Bonnet) and funded by the Flotte Océanographique Française, the A-MIDeX of the Aix-Marseille University, the LEFE-CYBER program and the ANR. We warmly thank all the scientists, the captain and the crew of the R/V L'Atalante for their cooperative work at sea. We thank Hélène Planquette for the pFe measurements and for reviewing this study. We thank Sandra Nunige for the processing of nutrients analyses. We thank Lise Artigue for her ingenious idea to couple eOMP and biogeochemical analyses.

Competing Interests

The authors declare that they have no conflict of interest.

References

Abadie, C., Lacan, F., Radic, A., Pradoux, C., & Poitrasson, F. (2017). Iron isotopes reveal distinct dissolved iron sources and pathways in the intermediate versus deep Southern Ocean. *Proceedings of the National Academy of Sciences*, *114*(5), 858-863. https://doi.org/10.1073/pnas.1603107114

Anderson, L. A., & Sarmiento, J. L. (1994). Redfield ratios of remineralization determined by nutrient data analysis. *Global Biogeochemical Cycles*, *8*(1), 65-80. https://doi.org/10.1029/93GB03318

Artigue, L., Lacan, F., van Gennip, S., Lohan, M. C., Wyatt, N. J., Woodward, E. M. S., Mahaffey, C., Hopkins, J., & Drillet, Y. (2020). Water mass analysis along 22 °N in the subtropical North Atlantic for the JC150 cruise (GEOTRACES, GApr08). *Deep Sea Research Part I: Oceanographic Research Papers*, *158*, 103230. https://doi.org/10.1016/j.dsr.2020.103230

Balistrieri, L., Brewer, P. G., & Murray, J. W. (1981). Scavenging residence times of trace metals and surface chemistry of sinking particles in the deep ocean. *Deep Sea Research Part A. Oceanographic Research Papers*, *28*(2), 101-121. https://doi.org/10.1016/0198-0149(81)90085-6

Barbeau, K., Rue, E. L., Trick, C. G., Bruland, K. W., & Butler, A. (2003). Photochemical reactivity of siderophores produced by marine heterotrophic bacteria and cyanobacteria based on characteristic Fe(III) binding groups. *Limnology and Oceanography*, *48*(3), 1069-1078. https://doi.org/10.4319/lo.2003.48.3.1069

Beghoura, H., Gorgues, T., Aumont, O., Planquette, H. F., Tagliabue, A., & Auger, P. -A. (2019). Impact of Inorganic Particles of Sedimentary Origin on Global Dissolved Iron and Phytoplankton Distribution. *Journal of Geophysical Research: Oceans*, *124*(12), 8626-8646. https://doi.org/10.1029/2019JC015119

Behrenfeld, M. J., & Milligan, A. J. (2013). Photophysiological Expressions of Iron Stress in Phytoplankton. *Annual Review of Marine Science*, *5*(1), 217-246. https://doi.org/10.1146/annurev-marine-121211-172356

Bennett, S. A., Achterberg, E. P., Connelly, D. P., Statham, P. J., Fones, G. R., & German, C. R. (2008). The distribution and stabilisation of dissolved Fe in deep-sea hydrothermal plumes. *Earth and Planetary Science Letters*, *270*(3-4), 157-167. https://doi.org/10.1016/j.epsl.2008.01.048

Bergquist, B. A., & Boyle, E. A. (2006). Dissolved iron in the tropical and subtropical Atlantic Ocean. *Global Biogeochemical Cycles*, *20*(1). https://doi.org/10.1029/2005GB002505

Beverskog, B., & Puigdomenech, I. (1996). Revised pourbaix diagrams for iron at 25–300 °C. *Corrosion Science*, *38*(12), 2121-2135. https://doi.org/10.1016/S0010-938X(96)00067-4

Black, E. E., Kienast, S. S., Lemaitre, N., Lam, P. J., Anderson, R. F., Planquette, H., Planchon, F., & Buesseler, K. O. (2020). Ironing Out Fe Residence Time in the Dynamic Upper Ocean. *Global Biogeochemical Cycles*, *34*(9). https://doi.org/10.1029/2020GB006592

Blain, S., Bonnet, S., & Guieu, C. (2008). Dissolved iron distribution in the tropical and sub tropical South Eastern Pacific. *Biogeosciences*, *5*(1), 269-280. https://doi.org/10.5194/bg-5-269-2008

Blain, S., Quéguiner, B., Armand, L., Belviso, S., Bombled, B., Bopp, L., Bowie, A., Brunet, C., Brussaard, C., Carlotti, F., Christaki, U., Corbière, A., Durand, I., Ebersbach, F., Fuda, J.-L., Garcia, N., Gerringa, L., Griffiths, B., Guigue, C., … Wagener, T. (2007). Effect of natural iron fertilization on carbon sequestration in the Southern Ocean. *Nature*, *446*(7139), 1070-1074. https://doi.org/10.1038/nature05700

Bonnet, S., Caffin, M., Berthelot, H., Grosso, O., Benavides, M., Helias-Nunige, S., Guieu, C., Stenegren, M., & Foster, R. A. (2018). In-depth characterization of diazotroph activity across the western tropical South Pacific hotspot of N₂ fixation (OUTPACE cruise). *Biogeosciences*, *15*(13), 4215-4232. https://doi.org/10.5194/bg-15-4215-2018

Bonnet, S., Caffin, M., Berthelot, H., & Moutin, T. (2017). Hot spot of N_2 fixation in the western tropical South Pacific pleads for a spatial decoupling between N_2 fixation and denitrification. *Proceedings of the National Academy of Sciences*, *114*(14), E2800-E2801. https://doi.org/10.1073/pnas.1619514114

Bonnet, S., Guieu, C., Bruyant, F., Prášil, O., Van Wambeke, F., Raimbault, P., Moutin, T., Grob, C., Gorbunov, M. Y., Zehr, J. P., Masquelier, S. M., Garczarek, L., & Claustre, H. (2008). Nutrient limitation of primary

productivity in the Southeast Pacific (BIOSOPE cruise). *Biogeosciences*, *5*(1), 215-225. https://doi.org/10.5194/bg-5-215-2008

Bostock, H. C., Sutton, P. J., Williams, M. J. M., & Opdyke, B. N. (2013). Reviewing the circulation and mixing of Antarctic Intermediate Water in the South Pacific using evidence from geochemical tracers and Argo float trajectories. *Deep Sea Research Part I: Oceanographic Research Papers*, *73*, 84-98. https://doi.org/10.1016/j.dsr.2012.11.007

Bowie, A. R., Achterberg, E. P., Mantoura, R. F. C., & Worsfold, P. J. (1998). Determination of sub-nanomolar levels of iron in seawater using flow injection with chemiluminescence detection. *Analytica Chimica Acta*, *361*(3), 189-200. https://doi.org/10.1016/S0003-2670(98)00015-4

Boyd, P. W., Ibisanmi, E., Sander, S. G., Hunter, K. A., & Jackson, G. A. (2010). Remineralization of upper ocean particles : Implications for iron biogeochemistry. *Limnology and Oceanography*, *55*(3), 1271-1288. https://doi.org/10.4319/lo.2010.55.3.1271

Boye, M., Nishioka, J., Croot, P., Laan, P., Timmermans, K. R., Strass, V. H., Takeda, S., & de Baar, H. J. W. (2010). Significant portion of dissolved organic Fe complexes in fact is Fe colloids. *Marine Chemistry*, *122*(1-4), 20-27. https://doi.org/10.1016/j.marchem.2010.09.001

Bressac, M., Guieu, C., Ellwood, M. J., Tagliabue, A., Wagener, T., Laurenceau-Cornec, E. C., Whitby, H., Sarthou, G., & Boyd, P. W. (2019). Resupply of mesopelagic dissolved iron controlled by particulate iron composition. *Nature Geoscience*, *6*(12), 995-1000. https://doi.org/10.1038/s41561-019-0476-6

Broecker, W. S. (1974). "NO", a conservative water-mass tracer. *Earth and Planetary Science Letters*, *23*(1), 100-107. https://doi.org/10.1016/0012-821X(74)90036-3

Bruland, K. W., Franks, R. P., Knauer, G. A., & Martin, J. H. (1979). Sampling and analytical methods for the determination of copper, cadmium, zinc, and nickel at the nanogram per liter level in sea water. *Analytica Chimica Acta*, *105*, 233-245. https://doi.org/10.1016/S0003-2670(01)83754-5

Bruland, K. W., & Lohan, M. C. (2006). 02. Controls of trace metals in seawater. In *Treatise on Geochemistry* (Vol. 6, p. 23-47).

Caffin, M., Moutin, T., Foster, R. A., Bouruet-Aubertot, P., Doglioli, A. M., Berthelot, H., Guieu, C., Grosso, O., Helias-Nunige, S., Leblond, N., Gimenez, A., Petrenko, A. A., de Verneil, A., & Bonnet, S. (2018). N_2 fixation as a dominant new N source in the western tropical South Pacific Ocean (OUTPACE cruise). *Biogeosciences*, *15*(8), 2565-2585. https://doi.org/10.5194/bg-15-2565-2018

Campbell, L., Carpenter, E., Montoya, J. P., Kustka, A., & Capone, D. G. (2005). Picoplankton community structure within and outside a Trichodesmium bloom in the southwestern Pacific Ocean. *Vie et Milieu*, *55*(3), 185-195.

Cohen, N. R., Noble, A. E., Moran, D. M., McIlvin, M. R., Goepfert, T. J., Hawco, N. J., German, C. R., Horner, T. J., Lamborg, C. H., McCrow, J. P., Allen, A. E., & Saito, M. A. (2021). *Hydrothermal trace metal release and microbial metabolism in the Northeast Lau Basin of the south Pacific Ocean* [Preprint]. Biogeochemistry: Environmental Microbiology. https://doi.org/10.5194/bg-2021-96

Conway, T. M., & John, S. G. (2014). Quantification of dissolved iron sources to the North Atlantic Ocean. *Nature*, *511*(7508), 212-215. https://doi.org/10.1038/nature13482

Cutter, G., Casciotti, K., Croot, P., Geibert, W., Heimbürger, L.-E., Lohan, M., Planquette, H., & Van De Flierdt, T. (2017). *Sampling and Sample-handling Protocols for GEOTRACES Cruises. Version 3, August 2017.* [139pp. & Appendices]. GEOTRACES International Project Office. https://doi.org/10.25607/OBP-2

de Ronde, C. E. J., Baker, E. T., Massoth, G. J., Lupton, J. E., Wright, I. C., Feely, R. A., & Greene, R. R. (2001). Intra-oceanic subduction-related hydrothermal venting, Kermadec volcanic arc, New Zealand. *Earth and Planetary Science Letters*, *193*(3-4), 359-369. https://doi.org/10.1016/S0012-821X(01)00534-9

Dick, G. J., Anantharaman, K., Baker, B. J., Li, M., Reed, D. C., & Sheik, C. S. (2013). The microbiology of deep-sea hydrothermal vent plumes : Ecological and biogeographic linkages to seafloor and water column habitats. *Frontiers in Microbiology*, *4*. https://doi.org/10.3389/fmicb.2013.00124

Dutheil, C., Aumont, O., Gorguès, T., Lorrain, A., Bonnet, S., Rodier, M., Dupouy, C., Shiozaki, T., & Menkes, C. (2018). *Modelling the processes driving <i>Trichodesmium</i> sp. Spatialdistribution and biogeochemical impact in the tropical PacificOcean* [Preprint]. Biogeochemistry: Modelling, Aquatic. https://doi.org/10.5194/bg-2017-559

Field, M. P., & Sherrell, R. M. (2000). Dissolved and particulate Fe in a hydrothermal plume at 9°45′N, East Pacific Rise: *Geochimica et Cosmochimica Acta*, *64*(4), 619-628. https://doi.org/10.1016/S0016-7037(99)00333-6

Fitzsimmons, J. N., Boyle, E. A., & Jenkins, W. J. (2014). Distal transport of dissolved hydrothermal iron in the deep South Pacific Ocean. *Proceedings of the National Academy of Sciences*, *111*(47), 16654-16661. https://doi.org/10.1073/pnas.1418778111

Fitzsimmons, J. N., Conway, T. M., Lee, J.-M., Kayser, R., Thyng, K. M., John, S. G., & Boyle, E. A. (2016). Dissolved iron and iron isotopes in the southeastern Pacific Ocean : Southeast Pacific Fe and Fe Isotopes. *Global Biogeochemical Cycles*, *30*(10), 1372-1395. https://doi.org/10.1002/2015GB005357

Fitzsimmons, J. N., John, S. G., Marsay, C. M., Hoffman, C. L., Nicholas, S. L., Toner, B. M., German, C. R., & Sherrell, R. M. (2017). Iron persistence in a distal hydrothermal plume supported by dissolved–particulate exchange. *Nature Geoscience*, *10*(3), 195-201. https://doi.org/10.1038/ngeo2900

Forsgren, G., Jansson, M., & Nilsson, P. (1996). Aggregation and Sedimentation of Iron, Phosphorus and Organic Carbon in Experimental Mixtures of Freshwater and Estuarine Water. *Estuarine, Coastal and Shelf Science*, *43*(2), 259-268. https://doi.org/10.1006/ecss.1996.0068

Ganachaud, A., Cravatte, S., Melet, A., Schiller, A., Holbrook, N. J., Sloyan, B. M., Widlansky, M. J., Bowen, M., Verron, J., Wiles, P., Ridgway, K., Sutton, P., Sprintall, J., Steinberg, C., Brassington, G., Cai, W., Davis, R., Gasparin, F., Gourdeau, L., … Send, U. (2014). The Southwest Pacific Ocean circulation and climate experiment (SPICE). *Journal of Geophysical Research: Oceans*, *119*(11), 7660-7686. https://doi.org/10.1002/2013JC009678

German, C. R., Casciotti, K. A., Dutay, J.-C., Heimbürger, L. E., Jenkins, W. J., Measures, C. I., Mills, R. A., Obata, H., Schlitzer, R., Tagliabue, A., Turner, D. R., & Whitby, H. (2016). Hydrothermal impacts on trace element and isotope ocean biogeochemistry. *Philosophical Transactions of the Royal Society A: Mathematical, Physical and Engineering Sciences*, *374*(2081), 20160035. https://doi.org/10.1098/rsta.2016.0035

Gledhill, M. (2012). The organic complexation of iron in the marine environment : A review. *Frontiers in Microbiology*, *3*. https://doi.org/10.3389/fmicb.2012.00069

Goldberg, E. D. (1954). Marine Geochemistry 1. Chemical Scavengers of the Sea. *The Journal of Geology*, *62*(3), 249-265. https://doi.org/10.1086/626161

González-Santana, D., González-Dávila, M., Lohan, M. C., Artigue, L., Planquette, H., Sarthou, G., Tagliabue, A., & Santana-Casiano, J. M. (2021). Variability in iron (II) oxidation kinetics across diverse hydrothermal sites on the northern Mid Atlantic Ridge. *Geochimica et Cosmochimica Acta*, *297*, 143-157. https://doi.org/10.1016/j.gca.2021.01.013

González-Santana, D., Planquette, H., Cheize, M., Whitby, H., Gourain, A., Holmes, T., Guyader, V., Cathalot, C., Pelleter, E., Fouquet, Y., & Sarthou, G. (2020). Processes Driving Iron and Manganese Dispersal From the TAG Hydrothermal Plume (Mid-Atlantic Ridge) : Results From a GEOTRACES Process Study. *Frontiers in Marine Science*, *7*, 568. https://doi.org/10.3389/fmars.2020.00568

González-Vega, A., Fraile-Nuez, E., Santana-Casiano, J. M., González-Dávila, M., Escánez-Pérez, J., Gómez-Ballesteros, M., Tello, O., & Arrieta, J. M. (2020). Significant Release of Dissolved Inorganic Nutrients From the Shallow Submarine Volcano Tagoro (Canary Islands) Based on Seven-Year Monitoring. *Frontiers in Marine Science*, *6*, 829. https://doi.org/10.3389/fmars.2019.00829

Guieu, C., & Bonnet, S. (2019). *TONGA cruise 2019, L'Atalante R/V*. https://doi.org/10.17600/18000884

Guieu, C., Bonnet, S., Petrenko, A., Menkes, C., Chavagnac, V., Desboeufs, K., Maes, C., & Moutin, T. (2018). Iron from a submarine source impacts the productive layer of the Western Tropical South Pacific (WTSP). *Scientific Reports*, *8*(1), 1-9. https://doi.org/10.1038/s41598-018-27407-z

Hawkes, J. A., Connelly, D. P., Rijkenberg, M. J. A., & Achterberg, E. P. (2014). The importance of shallow hydrothermal island arc systems in ocean biogeochemistry. *Geophysical Research Letters*, *41*(3), 942-947. https://doi.org/10.1002/2013GL058817

Hering, J. G., & Morel, F. M. M. (1990). Kinetics of trace metal complexation : Ligand-exchange reactions. *Environmental Science & Technology*, *24*(2), 242-252. https://doi.org/10.1021/es00072a014

Homoky, W. B., Weber, T., Berelson, W. M., Conway, T. M., Henderson, G. M., van Hulten, M., Jeandel, C., Severmann, S., & Tagliabue, A. (2016). Quantifying trace element and isotope fluxes at the ocean–sediment boundary : A review. *Philosophical Transactions of the Royal Society A: Mathematical, Physical and Engineering Sciences*, *374*(2081), 20160246. https://doi.org/10.1098/rsta.2016.0246

Hudson, A., Bender, M. L., & Graham, D. W. (1986). Iron enrichments in hydrothermal plumes over the East Pacific Rise. *Earth and Planetary Science Letters*, *79*(3-4), 250-254. https://doi.org/10.1016/0012-821X(86)90183-4

IPCC (Éd.). (2021). *Climate Change 2021 : The Physical Science Basis. Contribution of Working Group I to the Sixth Assessment Report of the Intergovernmental Panel on Climate Change*. Cambridge University Press.

John, S. G., & Adkins, J. (2012). The vertical distribution of iron stable isotopes in the North Atlantic near Bermuda. *Global Biogeochemical Cycles*, *26*(2). https://doi.org/10.1029/2011GB004043

Johnson, K. S., Coale, K. H., Elrod, V. A., & Tindale, N. W. (1994). Iron photochemistry in seawater from the equatorial Pacific. *Marine Chemistry*, *46*(4), 319-334. https://doi.org/10.1016/0304-4203(94)90029-9

Johnson, K. S., Gordon, R. M., & Coale, K. H. (1997). What controls dissolved iron concentrations in the world ocean? *Marine Chemistry*, *57*(3-4), 137-161. https://doi.org/10.1016/S0304-4203(97)00043-1

Kuma, K., Nakabayashi, S., Suzuki, Y., Kudo, I., & Matsunaga, K. (1992). Photo-reduction of Fe(III) by dissolved organic substances and existence of Fe(II) in seawater during spring blooms. *Marine Chemistry*, *37*(1-2), 15-27. https://doi.org/10.1016/0304-4203(92)90054-E

Labatut, M. (2014). *Apports continentaux de Fer à l'océan : Approche isotopique—Océan Pacifique Equatorial* [Océan, Atmosphère, Universite Toulouse III Paul Sabatier]. tel-01128617.

Landing, W. M., Haraldsson, Conny., & Paxeus, Nicklas. (1986). Vinyl polymer agglomerate based transition metal cation-chelating ion-exchange resin containing the 8-hydroxyquinoline functional group. *Analytical Chemistry*, *58*(14), 3031-3035. https://doi.org/10.1021/ac00127a029

Lilley, M. D., Feely, R. A., & Trefry, J. H. (2013). Chemical and Biochemical Transformations in Hydrothermal Plumes. In *Seafloor Hydrothermal Systems : Physical, Chemical, Biological, and Geological Interactions* (p. 369-391). American Geophysical Union (AGU). https://doi.org/10.1029/GM091p0369

Lory, C., Van Wambeke, F., Fourquez, M., Berman-Frank, I., Barani, A., Tilliette, C., Marie, D., Nunige, S., Guieu, C., & Bonnet, S. (2022). Assessing the contribution of diazotrophs to microbial Fe uptake using a group specific approach in the Western Tropical South Pacific. Article submitted for publication. *ISME COMMUN.*

Loscher, B. M., De Baar, H. J. W., De Jong, J. T. M., Veth, C., & Dehairs, F. (1997). The distribution of Fe in the antarctic circumpolar current. *Deep Sea Research Part II: Topical Studies in Oceanography*, *44*(1-2), 143-187. https://doi.org/10.1016/S0967-0645(96)00101-4

Lough, A. J. M., Homoky, W. B., Connelly, D. P., Comer-Warner, S. A., Nakamura, K., Abyaneh, M. K., Kaulich, B., & Mills, R. A. (2019). Soluble iron conservation and colloidal iron dynamics in a hydrothermal plume. *Chemical Geology*, *511*, 225-237. https://doi.org/10.1016/j.chemgeo.2019.01.001

Lupton, J. E., Pyle, D. G., Jenkins, W. J., Greene, R., & Evans, L. (2004). Evidence for an extensive hydrothermal plume in the Tonga-Fiji region of the South Pacific. *Geochemistry, Geophysics, Geosystems*, *5*(1). https://doi.org/10.1029/2003GC000607

Mahadevan, A. (2016). The Impact of Submesoscale Physics on Primary Productivity of Plankton. *Annual Review of Marine Science*, *8*(1), 161-184. https://doi.org/10.1146/annurev-marine-010814-015912

Maldonado, M. T., Strzepek, R. F., Sander, S., & Boyd, P. W. (2005). Acquisition of iron bound to strong organic complexes, with different Fe binding groups and photochemical reactivities, by plankton communities in Fe-limited subantarctic waters. *Global Biogeochemical Cycles*, *19*(4). https://doi.org/10.1029/2005GB002481

Martin, J. H. (1990). Glacial-interglacial CO_2 change : The Iron Hypothesis. *Paleoceanography*, *5*(1), 1-13. https://doi.org/10.1029/PA005i001p00001

Martin, J. H., Coale, K. H., Johnson, K. S., Fitzwater, S. E., Gordon, R. M., Tanner, S. J., Hunter, C. N., Elrod, V. A., Nowicki, J. L., Coley, T. L., Barber, R. T., Lindley, S., Watson, A. J., Van Scoy, K., Law, C. S., Liddicoat, M. I., Ling, R., Stanton, T., Stockel, J., … Tindale, N. W. (1994). Testing the iron hypothesis in ecosystems of the equatorial Pacific Ocean. *Nature*, *371*(6493), 123-129. https://doi.org/10.1038/371123a0

Massoth, G., Baker, E., Worthington, T., Lupton, J., de Ronde, C., Arculus, R., Walker, S., Nakamura, K., Ishibashi, J., Stoffers, P., Resing, J., Greene, R., & Lebon, G. (2007). Multiple hydrothermal sources along the south Tonga arc and Valu Fa Ridge. *Geochemistry, Geophysics, Geosystems*, *8*(11). https://doi.org/10.1029/2007GC001675

Menard, H. (1960). The East Pacific Rise. *Science*, *132*(3441), 1737-1746.

Miller, W. L., King, D. W., Lin, J., & Kester, D. R. (1995). Photochemical redox cycling of iron in coastal seawater. *Marine Chemistry*, *50*(1-4), 63-77. https://doi.org/10.1016/0304-4203(95)00027-O

Mills, M. M., Ridame, C., Davey, M., La Roche, J., & Geider, R. J. (2004). Iron and phosphorus co-limit nitrogen fixation in the eastern tropical North Atlantic. *Nature*, *429*(6989), 292-294. https://doi.org/10.1038/nature02550

Morris, P. J., & Charette, M. A. (2013). A synthesis of upper ocean carbon and dissolved iron budgets for Southern Ocean natural iron fertilisation studies. *Deep Sea Research Part II: Topical Studies in Oceanography*, *90*, 147-157. https://doi.org/10.1016/j.dsr2.2013.02.001

Moutin, T., & Bonnet, S. (2015). *OUTPACE cruise,L'Atalante R/V*. https://doi.org/10.17600/15000900

Moutin, T., Karl, D. M., Duhamel, S., Rimmelin, P., Raimbault, P., Van Mooy, B. A. S., & Claustre, H. (2008). Phosphate availability and the ultimate control of new nitrogen input by nitrogen fixation in the tropical Pacific Ocean. *Biogeosciences*, *5*(1), 95-109. https://doi.org/10.5194/bg-5-95-2008

Obata, H., Karatani, H., Matsui, M., & Nakayama, E. (1997). Fundamental studies for chemical speciation of iron in seawater with an improved analytical method. *Marine Chemistry*, *56*(1-2), 97-106. https://doi.org/10.1016/S0304-4203(96)00082-5

Peters, B. D., Jenkins, W. J., Swift, J. H., German, C. R., Moffett, J. W., Cutter, G. A., Brzezinski, M. A., & Casciotti, K. L. (2018). Water mass analysis of the 2013 US GEOTRACES eastern Pacific zonal transect (GP16). *Marine Chemistry*, *201*, 6-19. https://doi.org/10.1016/j.marchem.2017.09.007

Plank, S., Marchese, F., Genzano, N., Nolde, M., & Martinis, S. (2020). The short life of the volcanic island New Late'iki (Tonga) analyzed by multi-sensor remote sensing data. *Scientific Reports*, *10*(1), 22293. https://doi.org/10.1038/s41598-020-79261-7

Pollard, R., Sanders, R., Lucas, M., & Statham, P. (2007). The Crozet Natural Iron Bloom and Export Experiment (CROZEX). *Deep Sea Research Part II: Topical Studies in Oceanography*, *54*(18-20), 1905-1914. https://doi.org/10.1016/j.dsr2.2007.07.023

Raapoto, H., Martinez, E., Petrenko, A., Doglioli, A., Gorgues, T., Sauzède, R., Maamaatuaiahutapu, K., Maes, C., Menkes, C., & Lefèvre, J. (2019). Role of Iron in the Marquesas Island Mass Effect. *Journal of Geophysical Research: Oceans*, *124*(11), 7781-7796. https://doi.org/10.1029/2019JC015275

Raven, J. A., Evans, M. C. W., & Korb, R. E. (1999). The role of trace metals in photosynthetic electron transport in O_2-evolving organisms. *Photosynthesis Research*, *60*(2/3), 111-150. https://doi.org/10.1023/A:1006282714942

Redfield, A. C., Ketchum, B. H., & Richards, F. A. (1963). The influence of organisms on the composition of sea-water. In *The composition of seawater : Comparative and descriptive oceanography* (Vol. 2, p. 26-77). Interscience Publishers: New York.

Reid, J. L. (1997). On the total geostrophic circulation of the pacific ocean : Flow patterns, tracers, and transports. *Progress in Oceanography*, *39*(4), 263-352. https://doi.org/10.1016/S0079-6611(97)00012-8

Resing, J. A., Sedwick, P. N., German, C. R., Jenkins, W. J., Moffett, J. W., Sohst, B. M., & Tagliabue, A. (2015). Basin-scale transport of hydrothermal dissolved metals across the South Pacific Ocean. *Nature*, *523*(7559), 200-203. https://doi.org/10.1038/nature14577

Rijkenberg, M. J. A., Gerringa, L. J. A., Timmermans, K. J., Fischer, A. C., Carolus, V., Maas, L. R. M., Neale, P. J., & De Baar, H. J. W. (2003, avril). *The photoreduction of iron in seawater*. EGS - AGU - EUG Joint Assembly, Nice (France).

Rijkenberg, M. J. A., Slagter, H. A., Rutgers van der Loeff, M., van Ooijen, J., & Gerringa, L. J. A. (2018). Dissolved Fe in the Deep and Upper Arctic Ocean With a Focus on Fe Limitation in the Nansen Basin. *Frontiers in Marine Science*, *5*, 88. https://doi.org/10.3389/fmars.2018.00088

Rousselet, L., de Verneil, A., Doglioli, A. M., Petrenko, A. A., Duhamel, S., Maes, C., & Blanke, B. (2018). Large- to submesoscale surface circulation and its implications on biogeochemical/biological horizontal distributions during the OUTPACE cruise (southwest Pacific). *Biogeosciences*, *15*(8), 2411-2431. https://doi.org/10.5194/bg-15-2411-2018

Rudnick, R. L., & Gao, S. (2003). Composition of the Continental Crust. In *Treatise on Geochemistry* (p. 1-64). Elsevier. https://doi.org/10.1016/B0-08-043751-6/03016-4

Rue, E. L., & Bruland, K. W. (1995). Complexation of iron(III) by natural organic ligands in the Central North Pacific as determined by a new competitive ligand equilibration/adsorptive cathodic stripping voltammetric method. *Marine Chemistry*, *50*(1-4), 117-138. https://doi.org/10.1016/0304-4203(95)00031-L

Rue, E. L., & Bruland, K. W. (1997). The role of organic complexation on ambient iron chemistry in the equatorial Pacific Ocean and the response of a mesoscale iron addition experiment. *Limnology and Oceanography*, *42*(5), 901-910. https://doi.org/10.4319/lo.1997.42.5.0901

Sander, S. G., & Koschinsky, A. (2011). Metal flux from hydrothermal vents increased by organic complexation. *Nature Geoscience*, *4*(3), 145-150. https://doi.org/10.1038/ngeo1088

Shiozaki, T., Kodama, T., & Furuya, K. (2014). Large-scale impact of the island mass effect through nitrogen fixation in the western South Pacific Ocean. *Geophysical Research Letters*, *41*(8), 2907-2913. https://doi.org/10.1002/2014GL059835

Stoffers, P., Worthington, T. J., Schwarz-Schampera, U., Hannington, M. D., Massoth, G. J., Hekinian, R., Schmidt, M., Lundsten, L. J., Evans, L. J., Vaiomo'unga, R., & Kerby, T. (2006). Submarine volcanoes and high-temperature hydrothermal venting on the Tonga arc, southwest Pacific. *Geology*, *34*(6), 453. https://doi.org/10.1130/G22227.1

Sunda, W. G., & Huntsman, S. A. (1995). Iron uptake and growth limitation in oceanic and coastal phytoplankton. *Marine Chemistry*, *50*(1-4), 189-206. https://doi.org/10.1016/0304-4203(95)00035-P

Tagliabue, A., Bopp, L., Dutay, J.-C., Bowie, A. R., Chever, F., Jean-Baptiste, P., Bucciarelli, E., Lannuzel, D., Remenyi, T., Sarthou, G., Aumont, O., Gehlen, M., & Jeandel, C. (2010). Hydrothermal contribution to the oceanic dissolved iron inventory. *Nature Geoscience*, *3*, 252-256. http://dx.doi.org/10.1038/ngeo818

Tagliabue, A., Bowie, A. R., Boyd, P. W., Buck, K. N., Johnson, K. S., & Saito, M. A. (2017). The integral role of iron in ocean biogeochemistry. *Nature*, *543*(7643), 51-59. https://doi.org/10.1038/nature21058

Tagliabue, A., Bowie, A. R., DeVries, T., Ellwood, M. J., Landing, W. M., Milne, A., Ohnemus, D. C., Twining, B. S., & Boyd, P. W. (2019). The interplay between regeneration and scavenging fluxes drives ocean iron cycling. *Nature Communications*, *10*(1), 4960. https://doi.org/10.1038/s41467-019-12775-5

Tagliabue, A., Mtshali, T., Aumont, O., Bowie, A. R., Klunder, M. B., Roychoudhury, A. N., & Swart, S. (2012). A global compilation of dissolved iron measurements : Focus on distributions and processes in the Southern Ocean. *Biogeosciences*, *9*(6), 2333-2349. https://doi.org/10.5194/bg-9-2333-2012

Tagliabue, A., & Resing, J. (2016). Impact of hydrothermalism on the ocean iron cycle. *Philosophical Transactions of the Royal Society A: Mathematical, Physical and Engineering Sciences*, *374*(2081), 20150291. https://doi.org/10.1098/rsta.2015.0291

Talley, L. D., Sparrow, M., Chapman, P., & Gould, J. (2007). *Pacific Ocean*. National Oceanography Center.

Tarasov, V. G. (2006). Effects of Shallow-Water Hydrothermal Venting on Biological Communities of Coastal Marine Ecosystems of the Western Pacific. In *Advances in Marine Biology* (Vol. 50, p. 267-421). Elsevier. https://doi.org/10.1016/S0065-2881(05)50004-X

Tomczak, M. (1999). Some historical, theoretical and applied aspects of quantitative water mass analysis. *Journal of Marine Research*, *57*(2), 275-303. https://doi.org/10.1357/002224099321618227

Tomczak, M., & Godfrey, J. S. (2003). *Regional oceanography : An introduction* (2. ed). Daya Publ. House.

Tomczak, M., & Large, D. G. B. (1989). Optimum multiparameter analysis of mixing in the thermocline of the eastern Indian Ocean. *Journal of Geophysical Research*, *94*(C11), 16141. https://doi.org/10.1029/JC094iC11p16141

Turekian, K. K. (1977). The fate of metals in the oceans. *Geochimica et Cosmochimica Acta*, *41*(8), 1139-1144. https://doi.org/10.1016/0016-7037(77)90109-0

van den Berg, C. M. G. (1995). Evidence for organic complexation of iron in seawater. *Marine Chemistry*, *50*(1-4), 139-157. https://doi.org/10.1016/0304-4203(95)00032-M

Von Damm, K. L. (1990). Seafloor hydrothermal activity : Black smoker chemistry and chimneys. *Annual Review of Earth and Planetary Sciences*, *18*(1), 173-204.

Webb, D. J. (2000). Evidence for Shallow Zonal Jets in the South Equatorial Current Region of the Southwest Pacific. *Journal of Physical Oceanography*, *30*(4), 706-720. https://doi.org/10.1175/1520-0485(2000)030<0706:EFSZJI>2.0.CO;2

Wu, J., Wells, M. L., & Rember, R. (2011). Dissolved iron anomaly in the deep tropical–subtropical Pacific : Evidence for long-range transport of hydrothermal iron. *Geochimica et Cosmochimica Acta*, *75*(2), 460-468. https://doi.org/10.1016/j.gca.2010.10.024

Yücel, M., Gartman, A., Chan, C. S., & Luther, G. W. (2011). Hydrothermal vents as a kinetically stable source of iron-sulphide-bearing nanoparticles to the ocean. *Nature Geoscience*, *4*(6), 367-371. https://doi.org/10.1038/ngeo1148

Global Biogeochemical Cycles

Supporting Information for

C. Tilliette[1*], V. Taillandier[1], P. Bouruet-Aubertot[2], N. Grima[3], C. Maes[3], M. Montanes[1], G. Sarthou[4], M-E. Vorrath[5], V. Arnone[6], M. Bressac[1], D. González-Santana[4], F. Gazeau[1] and C. Guieu[1*]

[1]Sorbonne Université, CNRS, Laboratoire d'Océanographie de Villefranche, LOV, 06230, Villefranche-sur-Mer, France

[2]Sorbonne Université, CNRS, IRD, Laboratoire d'Océanographie et de Climatologie par Expérimentation et Approche Numérique (LOCEAN), Paris, France

[3]Univ Brest, CNRS, IRD, Ifremer Laboratoire d'Océanographie Physique et Spatiale (LOPS, UMR 6523), IUEM, Brest, France

[4]Univ Brest, CNRS, IRD, Ifremer, LEMAR, F-29280 Plouzane, France

[5]Alfred Wegener Institute, Helmholtz Centre for Polar and Marine Research, 27568 Bremerhaven, Germany

[6]Instituto de Oceanografía y Cambio Global, IOCAG, Universidad de Las Palmas de Gran Canaria, ULPGC, 35017 Las Palmas de Gran Canaria, Spain

[*]Corresponding author: Chloé Tilliette (chloe.tilliette@imev-mer.fr) and Cécile Guieu (cecile.guieu@imev-mer.fr)

Contents of this file

Introduction

Text S1 describes the complete methodology of the Lagrangian Particle Tracking Experiments (LPTE). Text S2 describes the methodology used to estimate the total vertical fluxes at LD 5-T5. Text S3 describes the sampling and analytical protocol used to measure particulate iron.

Figure S1 contains the temperature-parameter profiles that allowed the identification of the end members for the extended optimum multiparameter analysis (eOMP). Figure S2 presents the residuals obtained for each parameter from the eOMP along the cruise section. Figure S3 represents the property-property profiles of the dataset used for the eOMP and the properties of the defined end-members. Figures S4-S5-S6 compile the results of the Lagrangian Particle Tracking Experiment (LPTE) for the eastern, central, and western portions of the cruise transect, respectively. Figures S7 and S8 show the trajectories of the SVP drifters and Argo floats, respectively.

Table S1 lists the analytical conditions and validation of the dissolved iron (dFe) measurements by Flow Injection Analysis and Chemiluminescence detection (FIA-CL). Table S2 includes descriptions of the three LPTE analyses performed and associated statistics. Table S3 lists the dissolved iron data sampled during the cruise as well as the particulate iron data used to estimate the scavenging process in the budget.

Text S1. Lagrangian Particle Tracking Experiment

To strengthen the eOMP analysis, a Lagrangian Particle Tracking Experiment (LPTE) was conducted to determine the main origin of the water masses crossing the cruise transect and thus ensure the robustness and reliability of the defined end-member zones. The Ariane Lagrangian analysis software (http://www.univ-brest.fr/lpo/ariane) and a numerical dataset from a global ocean circulation model were used to perform this analysis. This approach is similar to that performed by Artigue et al. (2020), however, a different method for seeding the numerical particles was chosen.

The dataset consists of 3D current fields (U, V and W) from the ORCA025 configuration of the Nucleus for European Modelling of the Ocean (NEMO; Gurvan et al., 2019). The horizontal resolution is 1/4° (~27 km at the equator, with 1442 points in longitude and 1021 in latitude) and the number of vertical levels is 75 with a higher resolution at the surface (i.e., ~1 m thick for the first vertical levels) that decreases towards the deep ocean (i.e., ~200 m thick for the last vertical levels). To represent the bottom topography more accurately in the model, partial steps were used for the water column bottom grid cells. Current fields are available monthly from January 1958 to December 2015. Details, specifics, and validation of the ORCA025 configuration can be found in Barnier et al. (2006).

The Ariane application (Blanke & Raynaud, 1997) allows the exact computation of 3D trajectories of numerical particles in stationary and non-divergent transport fields defined on a C-grid (Arakawa & Lamb, 1977). Following an algorithm described by Blanke et al. (1999), it is possible to deduce from these trajectories the exact current function that describes the path traveled and the intensity of water masses from one section to another. Ariane proposes either to position the numerical particles "by hand" in the same way as Artigue et al. (2020), or as we chose in this study, to let the application automatically instrument the transport from an initial section where the particles will be released (this section was defined as vertical at the level of the cruise transect), to final particle interception sections (also vertical) sufficiently far from the transect to contain the eOMP end-members.

The initial section circumscribing the cruise transect is represented by red rectangles centered at latitude 20 °S and defined between longitudes 175 °E and 165 °W (see Figs. S3-S4-S5). Interception sections, sufficiently spaced to contain the end-members, surround the initial section to the north (16 °N), east (70 °W), south (60 °S), and west (150 °E) of the Pacific Ocean (see Figs. S4-S5-S6). While surface water mass transport between the end-member zone and the cruise transect is generally quite rapid (i.e., a few years to a few decades), transfer times can range from decades to hundreds of years for intermediate and deep waters. We therefore chose to loop the time series six times from 1958 to 2015 (58 years) to obtain a 348-year time series. We set up the Ariane application to instrument the initial section monthly for the last five years of our time series and to integrate the backward trajectories. The initial section, representing the cruise near-latitudinal transect, is subdivided into three sections following longitude: the western part (i.e., Melanesian waters comprising SD 2 and 3; 175 °E-179 °W), the central part (i.e., Lau Basin including SD 4, 11 and 12 as well as LD 5 and 10; 179-174.5 °W) and the eastern part

(i.e., South Pacific gyre comprising SD 6, 7 and 8; 174.5-165 °W). Vertical sections corresponding to each end-member were also defined at five depth ranges: between 0-258 m (STUW), 258-536 m (WSPCW), 536-1583 m (AAIW), 1583-3418 m (PDW) and > 3418 m (LCDW). All this information is summarized in Table S2, which also displays the statistics of the quantitative results of our Lagrangian analysis.

Text S2. Quantification of total vertical fluxes at LD 5-T5

For this purpose, it was assumed that the rate of change of dFe concentration can be described by a one-dimensional reaction-advection-diffusion equation:

$$\omega \frac{dC}{dz} - \frac{d}{dz}\left(D_z \frac{dC}{dz}\right) = R$$

where z is the depth (m), C is the dFe concentration (nmol kg^{-1}), ω is the vertical velocity (m s^{-1} in the positive downward direction), D_z is the eddy diffusivity (m^2 s^{-1}) and R is the net production rate (nmol kg^{-1} d^{-1}). Negative production rates indicate consumption of dFe.

An intermediate layer was targeted between the depleted layer at the surface (0-90 m) and the enriched layer above the seafloor (150-200 m). Horizontal transport fluxes were assumed to be negligible in this layer, supposedly less dynamically active than the surface and bottom layers.

The "Rate Estimation from Concentration" model developed by Lettmann et al. (2012) was used to estimate the R profiles, providing the inputs for the C, ω and D_z profiles in the 90-150 m depth range. The C and D_z profiles were measured *in situ* whereas ω was specified upward, with a large intensity in the lower part and a very small intensity in the upper part, leading to values of -10^{-5} m s^{-1} below 140 m and -2.10^{-8} m s^{-1} above 130 m, respectively. Boundary conditions were specified as buffer concentrations in the depleted surface layer (0 nmol dFe kg^{-1}) and in the enriched bottom layer (40 nmol dFe kg^{-1}).

The modeled dFe and rate profiles were determined to satisfy equilibrium given the inputs profiles. Total fluxes (advective and diffusive) across the upper and lower boundaries were also estimated by the model.

Text S3. Sampling and analytical protocol for particulate iron measurement

Seawater samples were collected according to the GEOTRACES guidelines (http://www.geotraces.org/images/Cookbook.pdf) from depth profiles using 24 GO-FLO bottles (12 L) with a Teflon inner coating. Bottles were mounted on a Trace Metal clean Rosette (TMR, General Oceanics Inc., Model 1018 Intelligent Rosette) attached to a 6 mm Kevlar® line. Sample bottles and equipment cleaning protocols also followed the GEOTRACES cookbook. Upon recovery of the TMR on board, the entire rosette was transferred inside a trace-metal clean ISO-7 container equipped with a class 100 laminar flow hood. The bottles were inverted three times to avoid particle sedimentation and

pressurized to < 8 psi with 0.2 µm filtered dinitrogen (N_2, Air Liquide®). Samples for particulate iron (pFe) were collected on acid-cleaned 0.45 µm pore-size polyethersulfone filters (Supor®, 25 mm) mounted on Swinnex® filter holders, following Planquette & Sherrell (2012). Samples were then stored frozen at -20 °C until digestion and analysis.

Total particle digestion was performed in a clean-room according to Planquette & Sherrell (2012). PFe measurements were performed by an Element XR™ high-resolution sector field inductively coupled plasma mass spectrometry (HR-SF-ICP-MS) instrument (Thermo Fisher, Bremen, Germany) at the Pôle Spectrométrie Océan (IFREMER, France). The method employed was similar to that of Planquette & Sherrell (2012). Particulate iron data used in this study are available in Table S3.

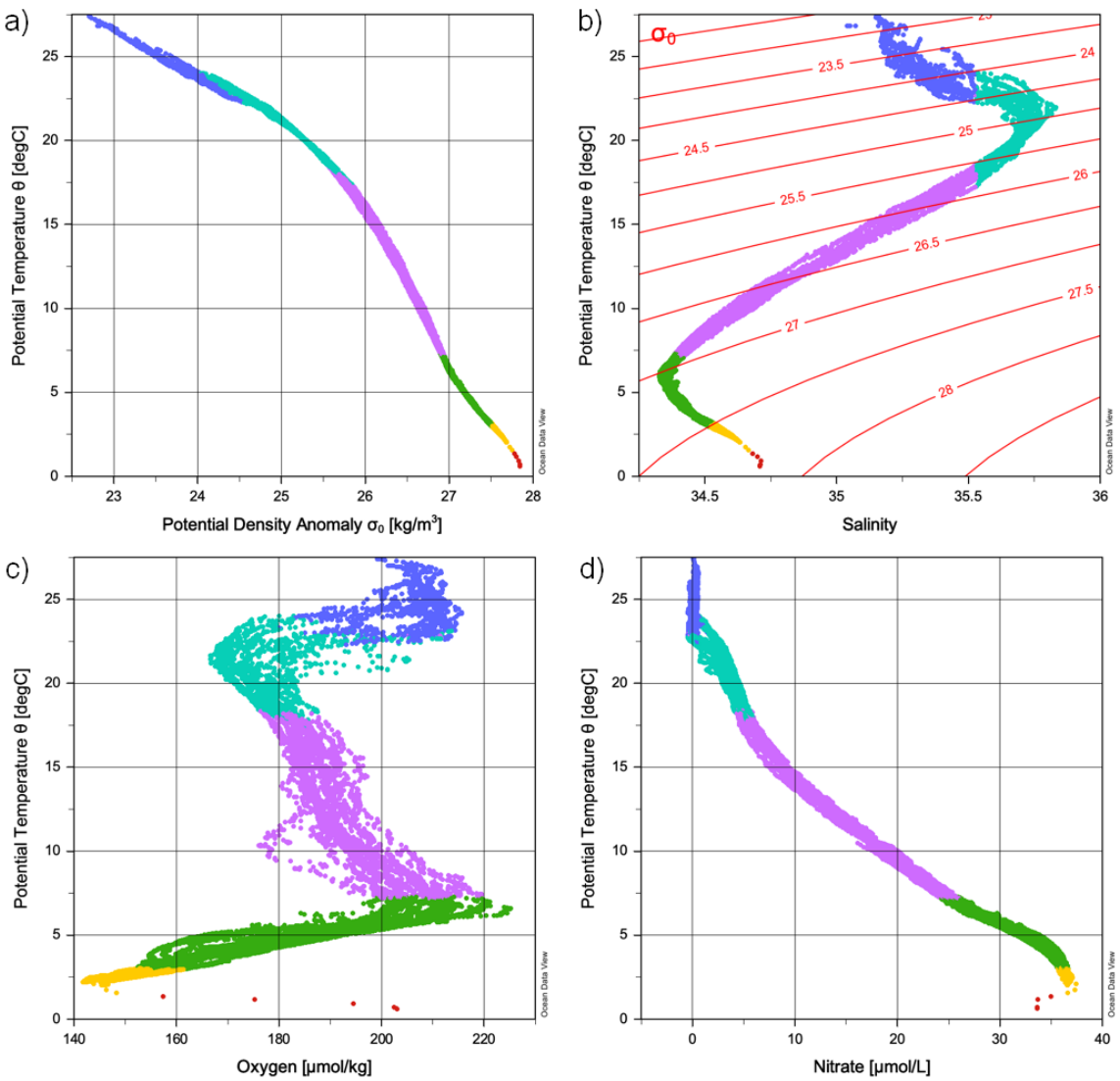

Figure S1. Property-property profiles used to identify water masses (i.e., end-members) suspected of contributing to the cruise transect. These profiles contain the full dataset collected for each parameter during the cruise. Temperature (°C) was plotted with (**a**) potential density anomaly (kg m^{-3}), (**b**) salinity, (**c**) oxygen (µmol kg^{-1}) and (**d**) nitrate concentrations (µmol L^{-1}). Colors represent the layers of each distinct water mass: light blue for the surface waters (ASW), cyan for the Subtropical Underwater (STUW), purple for the Western South Pacific Central Water (WSPCW), green for the Antarctic Intermediate Water (AAIW), yellow for the Pacific Deep Water (PDW) and red for the Lower Circumpolar Deep Water (LCDW).

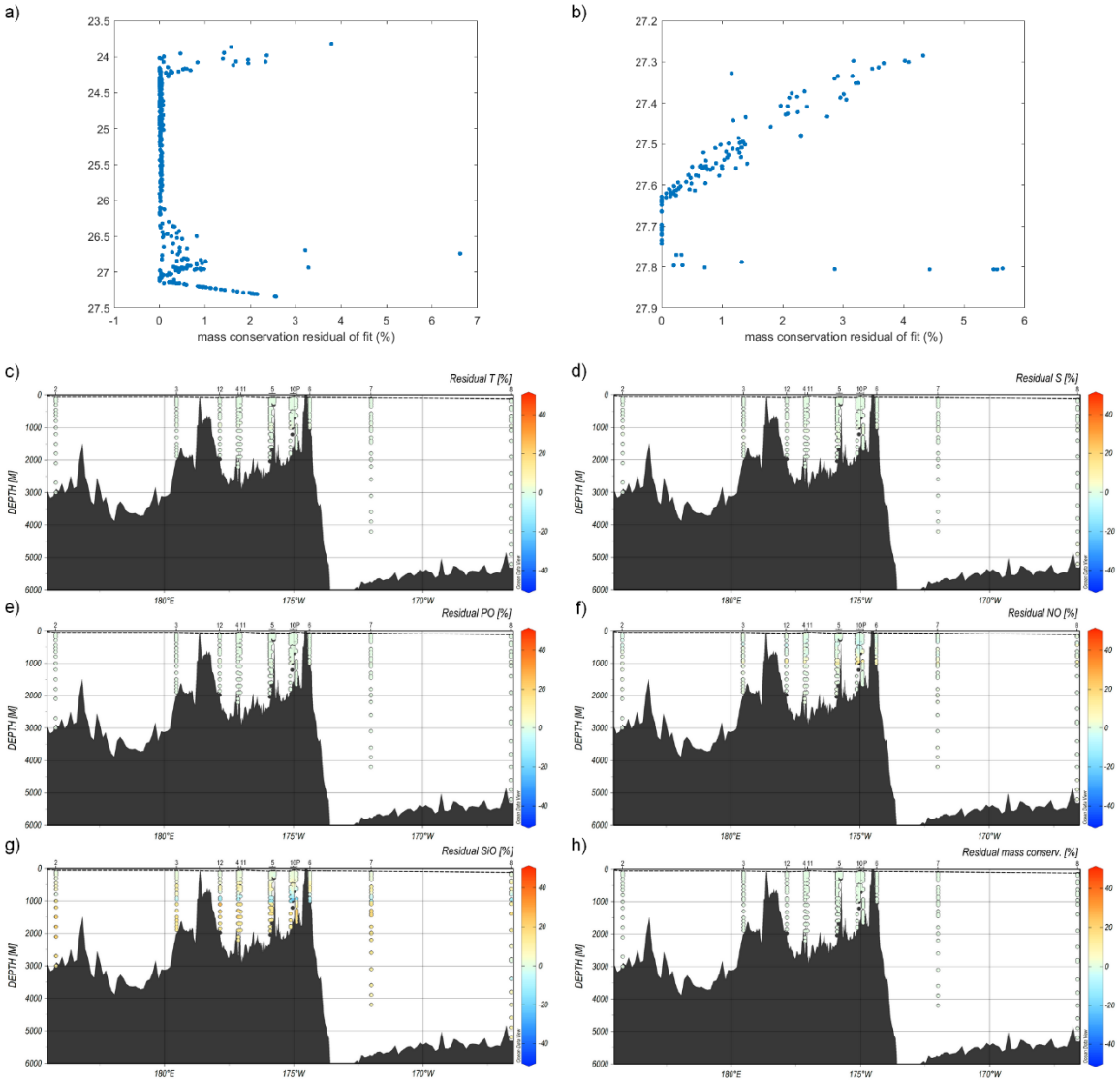

Figure S2. Residuals expressed as a percentage of the two vertical domains in which the extended optimum multiparameter analysis (eOMP) was performed independently: **(a)** upper and **(b)** lower domains. Sections present residuals in % of temperature **(c)**, salinity **(d)**, PO **(e)**, NO **(f)**, SiO **(g)** and mass conservation **(h)** along the transect. Note that obtaining calculated hydrographic properties greater than those observed leads to positive residual values and conversely for negative residual values. The black dotted line represents the limit above which the eOMP could not be applied (i.e., due to non-conservative parameters in the surface layer and residuals > 5%). The black dots represent the samples for which the eOMP could not be performed.

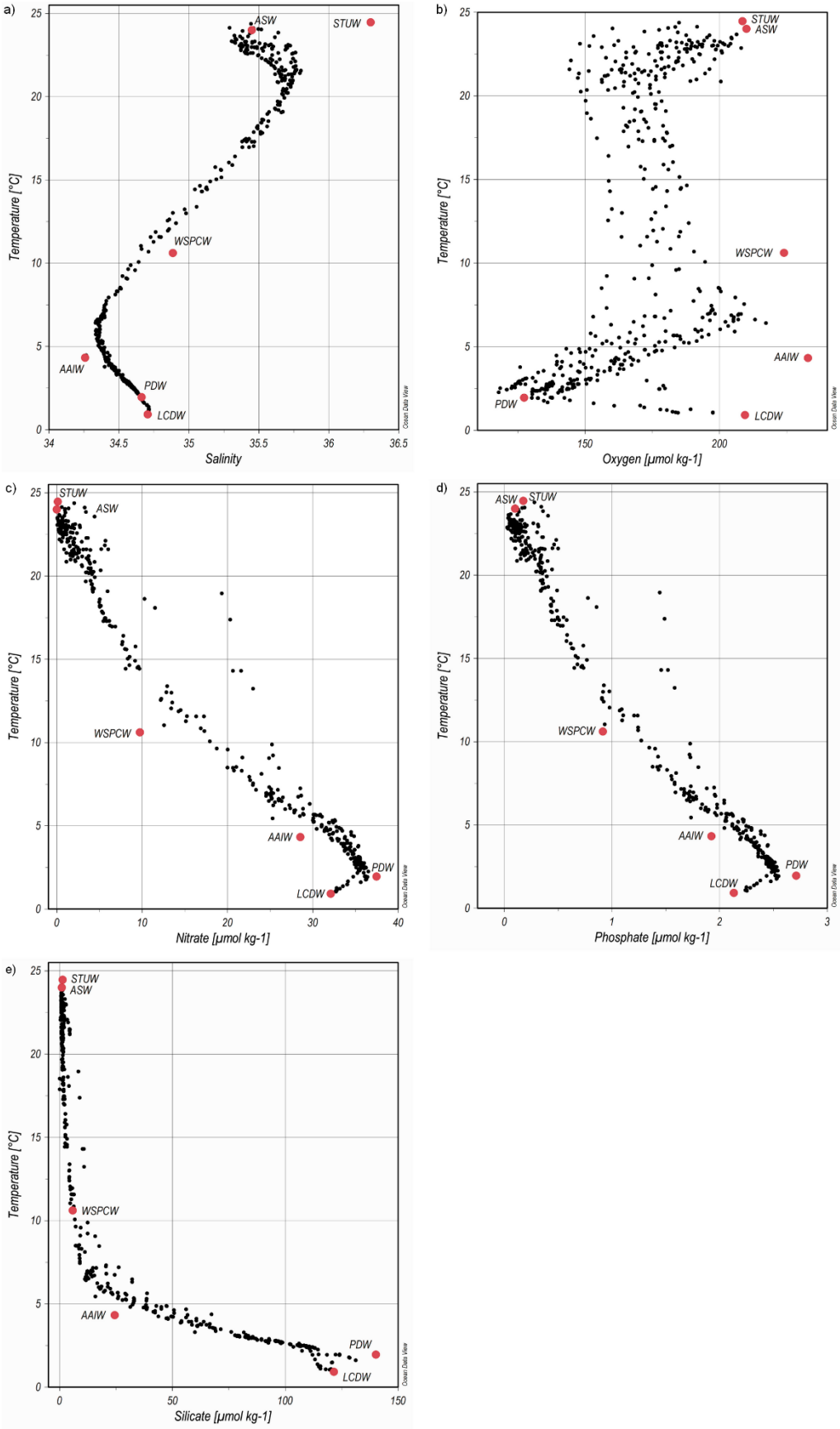
a)
Temperature [°C]
Salinity
ASW
STUW
WSPCW
AAIW
PDW
LCDW
b)
Temperature [°C]
Oxygen [µmol kg-1]
STUW
ASW
WSPCW
AAIW
PDW
LCDW
c)
Temperature [°C]
Nitrate [µmol kg-1]
STUW
ASW
WSPCW
AAIW
PDW
LCDW
d)
Temperature [°C]
Phosphate [µmol kg-1]
ASW
STUW
WSPCW
AAIW
PDW
LCDW
e)
Temperature [°C]
Silicate [µmol kg-1]
STUW
ASW
WSPCW
AAIW
PDW
LCDW
Ocean Data View

Figure S3. Temperature-property profiles as a function of **(a)** salinity, **(b)** oxygen (µmol kg^{-1}), **(c)** nitrate (µmol kg^{-1}), **(d)** phosphate (µmol kg^{-1}) and **(e)** silicate (µmol kg^{-1}) concentrations from the cruise dataset used for the eOMP analysis (black dots). The red dots represent the properties of the defined end-members. See Fig. S1 for end-member acronyms. The complete dataset is available in the LEFE-CYBER database.

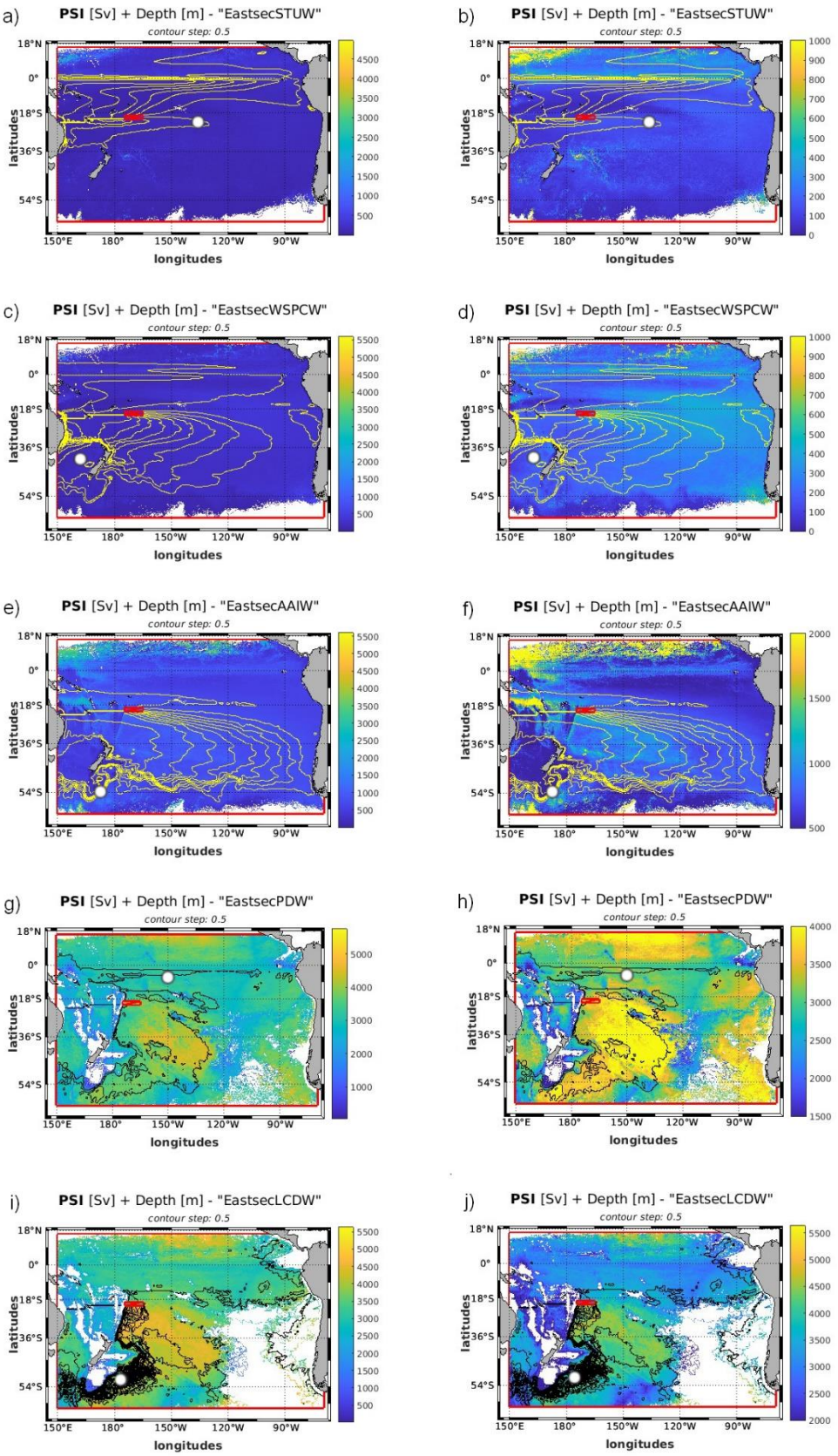
a)
PSI [Sv] + Depth [m] - "EastsecSTUW"
contour step: 0.5
b)
PSI [Sv] + Depth [m] - "EastsecSTUW"
contour step: 0.5
c)
PSI [Sv] + Depth [m] - "EastsecWSPCW"
contour step: 0.5
d)
PSI [Sv] + Depth [m] - "EastsecWSPCW"
contour step: 0.5
e)
PSI [Sv] + Depth [m] - "EastsecAAIW"
contour step: 0.5
f)
PSI [Sv] + Depth [m] - "EastsecAAIW"
contour step: 0.5
g)
PSI [Sv] + Depth [m] - "EastsecPDW"
contour step: 0.5
h)
PSI [Sv] + Depth [m] - "EastsecPDW"
contour step: 0.5
i)
PSI [Sv] + Depth [m] - "EastsecLCDW"
contour step: 0.5
j)
PSI [Sv] + Depth [m] - "EastsecLCDW"
contour step: 0.5
latitudes
longitudes
18°N
0°
18°S
36°S
54°S
150°E
180°
150°W
120°W
90°W

Figure S4. Particle trajectories computed by the Lagrangian Particle Tracking Experiment (LPTE) showing the origin of the particles and the most common paths used to reach the eastern part of the transect (*i.e.*, South Pacific gyre). Results are presented for each end-member with two different depth scales: STUW over the entire water column depth **(a)** and between 0 and 1000 m **(b)**, WSPCW over the entire water column depth **(c)** and between 0 and 1000 m **(d)**, AAIW over the entire water column depth **(e)** and between 500 and 2000 m **(f)**, PDW over the entire water column depth **(g)** and between 1500 and 4000 m **(h)** and LCDW over the entire water column depth **(i)** and between 2000 and 5500 m **(j)**. The red rectangle represents the eastern portion of the cruise transect (from 174.5 to 165 °W), centered at 20 °S and including SD 6, 7 and 8. The yellow and black lines represent the main trajectories of the particles. The white circle on each graph represents the position of the analyzed end-member. The red lines represent the interception sections surrounding the initial section to the north (16 °N), east (70 °W), south (60 °S), and west (150 °E) of the Pacific Ocean.

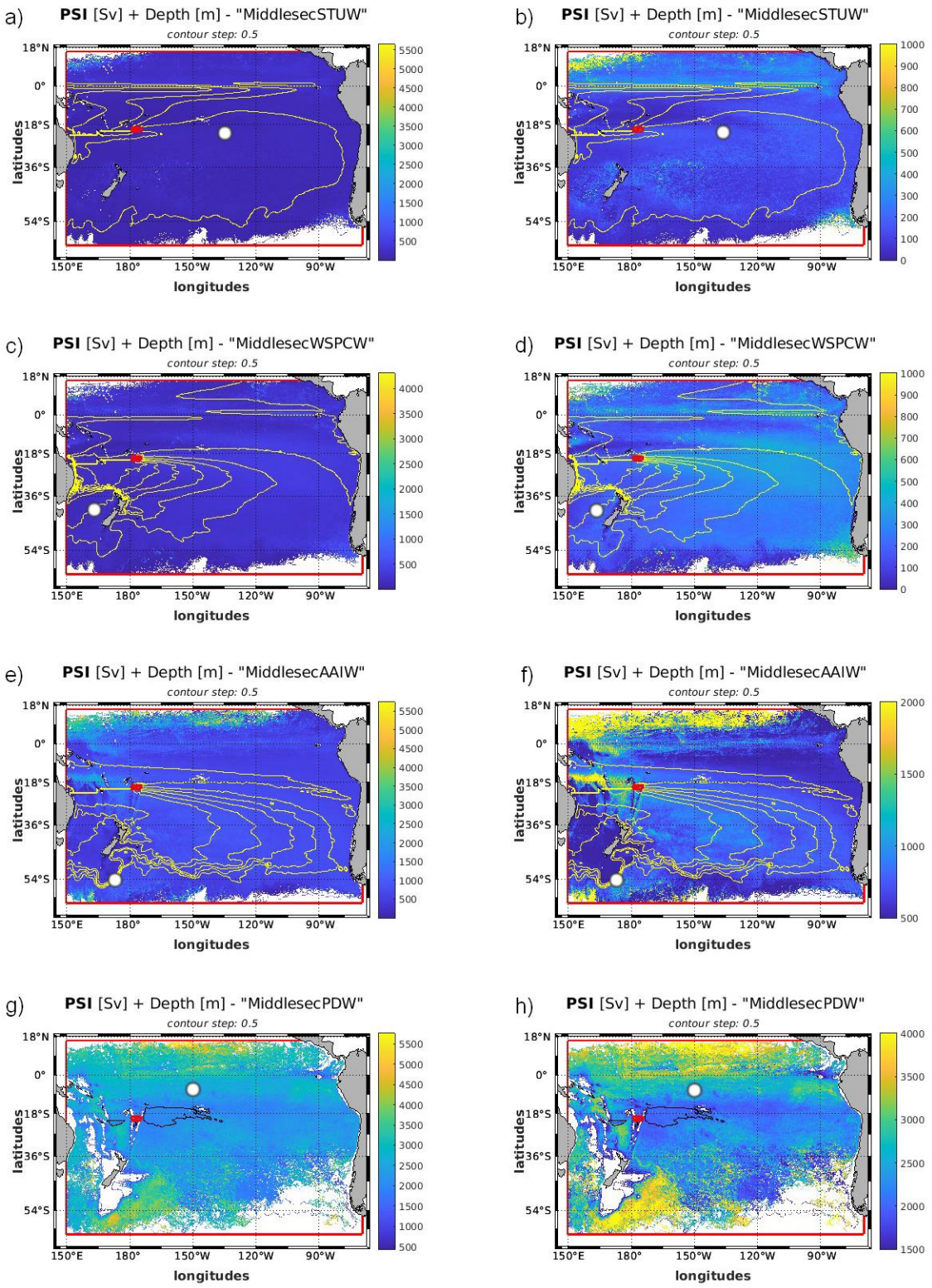

Figure S5. Particle trajectories computed by the Lagrangian Particle Tracking Experiment (LPTE) showing the origin of the particles and the most common paths used to reach the

middle part of the transect (*i.e.*, Lau Basin). Results are presented for each end-member with two different depth scales: STUW over the entire water column depth **(a)** and between 0 and 1000 m **(b)**, WSPCW over the entire water column depth **(c)** and between 0 and 1000 m **(d)**, AAIW over the entire water column depth **(e)** and between 500 and 2000 m **(f)** and PDW over the entire water column depth **(g)** and between 1500 and 4000 m **(h)**. The red rectangle represents the central portion of the cruise transect (from 179 to 174.5 °W), centered at 20 °S and including SD 4, 11 and 12 as well as LD 5 and 10. The yellow and black lines represent the main trajectories of the particles. The white circle on each graph represents the position of the analyzed end-member. Note that LDCW was too deep relative to the Lau Basin seafloor (central portion of the transect) and therefore was not incorporated into this LPTE analysis. The red lines represent interception sections surrounding the initial section to the north (16 °N), east (70 °W), south (60 °S), and west (150 °E) of the Pacific Ocean.

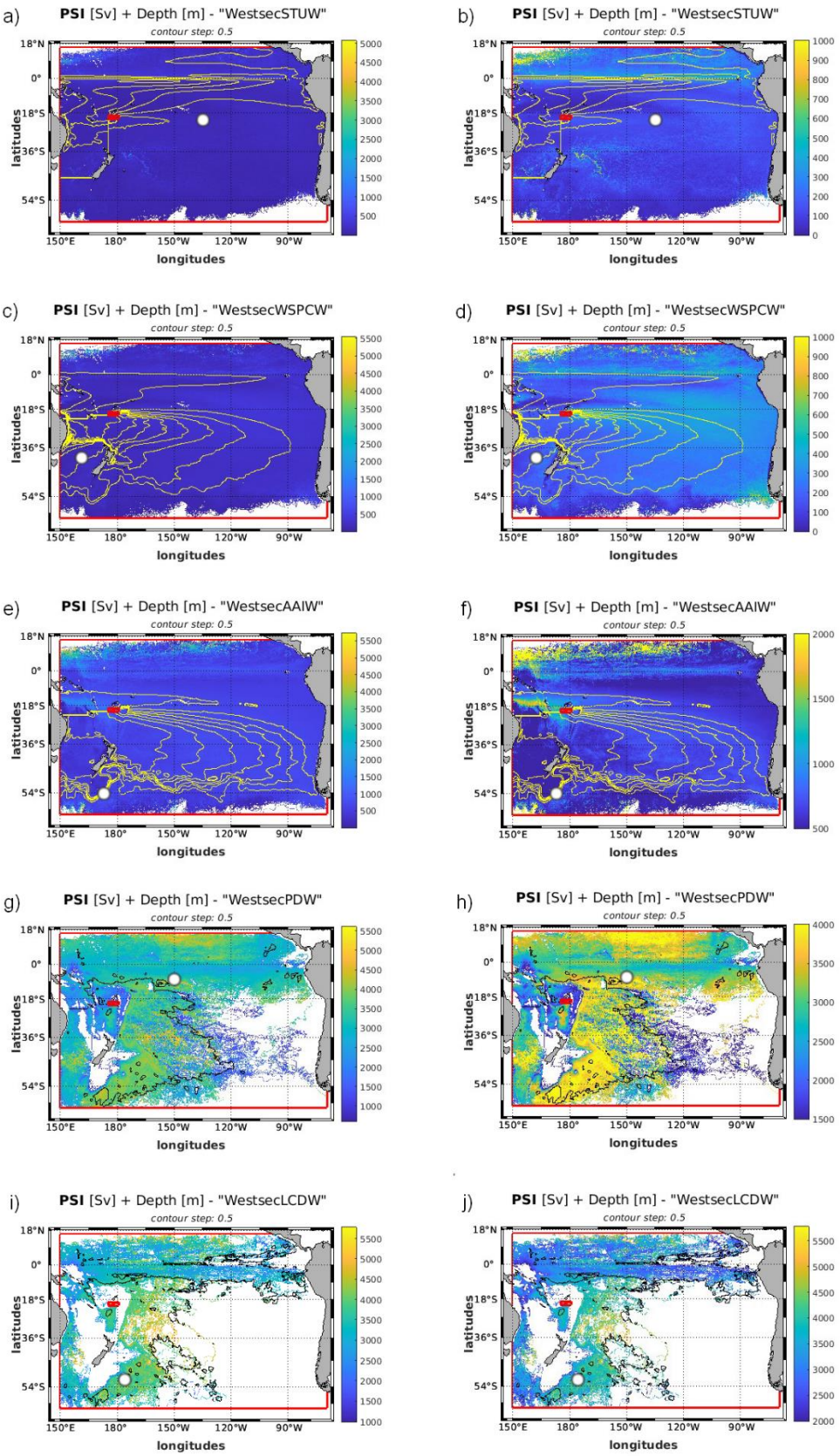
a)
PSI [Sv] + Depth [m] - "WestsecSTUW"
contour step: 0.5
b)
PSI [Sv] + Depth [m] - "WestsecSTUW"
contour step: 0.5
c)
PSI [Sv] + Depth [m] - "WestsecWSPCW"
contour step: 0.5
d)
PSI [Sv] + Depth [m] - "WestsecWSPCW"
contour step: 0.5
e)
PSI [Sv] + Depth [m] - "WestsecAAIW"
contour step: 0.5
f)
PSI [Sv] + Depth [m] - "WestsecAAIW"
contour step: 0.5
g)
PSI [Sv] + Depth [m] - "WestsecPDW"
contour step: 0.5
h)
PSI [Sv] + Depth [m] - "WestsecPDW"
contour step: 0.5
i)
PSI [Sv] + Depth [m] - "WestsecLCDW"
contour step: 0.5
j)
PSI [Sv] + Depth [m] - "WestsecLCDW"
contour step: 0.5
latitudes
longitudes
18°N
0°
18°S
36°S
54°S
150°E
180°
150°W
120°W
90°W

Figure S6. Particle trajectories computed by the Lagrangian Particle Tracking Experiment (LPTE) showing the origin of the particles and the most common paths used to reach the western part of the transect (*i.e.*, Melanesian waters). Results are presented for each end-member with two different depth scales: STUW over the entire water column depth **(a)** and between 0 and 1000 m **(b)**, WSPCW over the entire water column depth **(c)** and between 0 and 1000 m **(d)**, AAIW over the entire water column depth **(e)** and between 500 and 2000 m **(f)**, PDW over the entire water column depth **(g)** and between 1500 and 4000 m **(h)** and LCDW over the entire water column depth **(i)** and between 2000 and 5500 m **(j)**. The red rectangle represents the western portion of the cruise transect (from 175 °E to 174.5 °W), centered at 20 °S and including SD 2 and 3. The yellow and black lines represent the main trajectories of the particles. The white circle on each graph represents the position of the analyzed end-member. The red lines represent interception sections surrounding the initial section to the north (16 °N), east (70 °W), south (60 °S), and west (150 °E) of the Pacific Ocean.

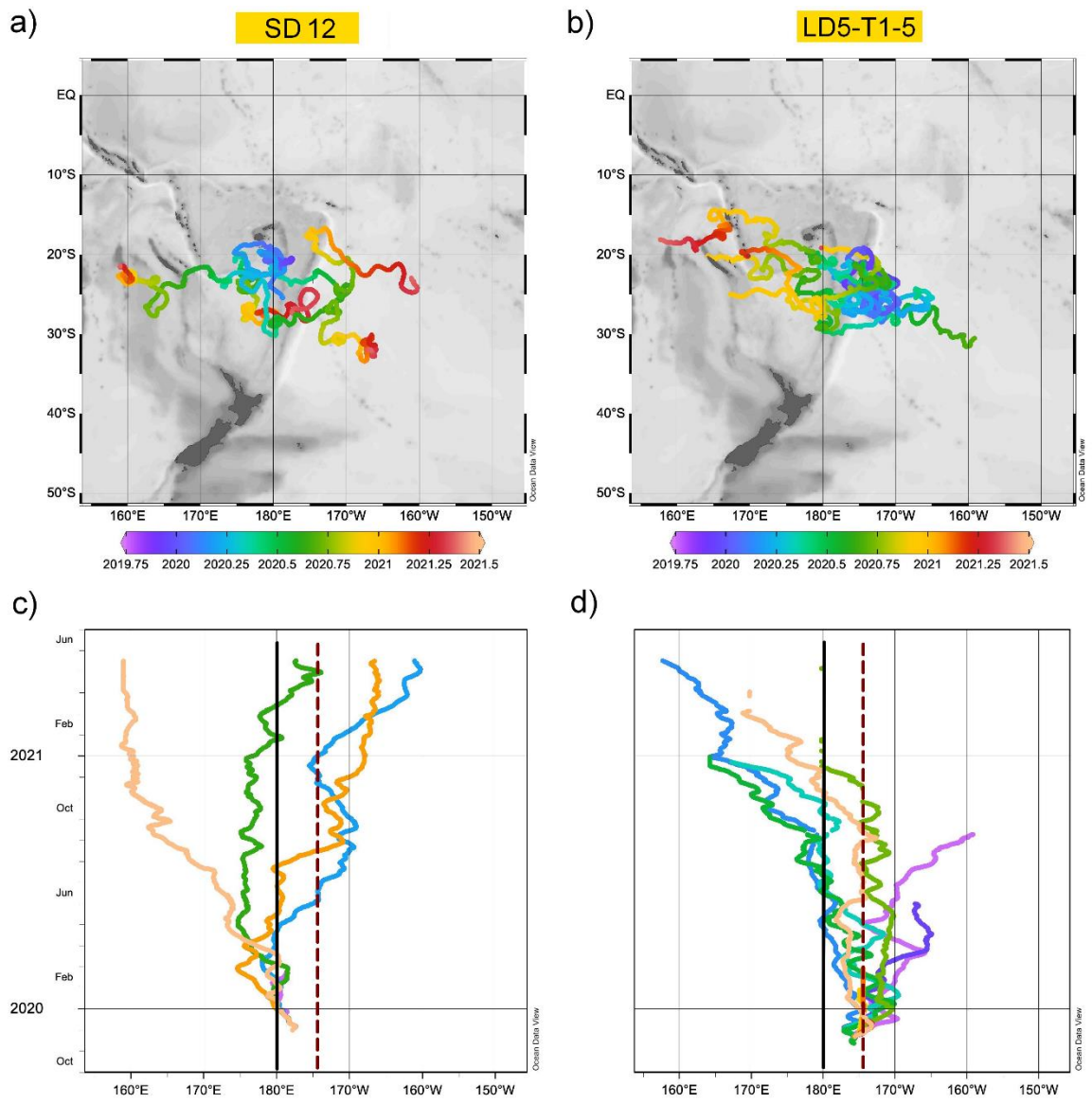

Figure S7. Trajectories of SVP drifters released during the cruise at SD 12 **(a, c)** and at LD 5-T1 and LD 5-T5 **(b, d)**. The two maps represent the 15 m-depth trajectories of all SVP drifters released at SD 12 **(a)** and at LD 5-T5 and LD 5-T1 **(b)** as a function of time. The graphs represent the unique trajectories as a function of time of each drifter released at SD 12 **(c)** and at LD 5-T5 and LD 5-T1 **(d)**, with each color corresponding to the trajectory of one drifter. The black line represents the Lau arc, the red dotted line represents the Tonga arc and the space between the two lines represents the Lau Basin. The laminar departure trajectory in the Lau Basin of the drifters released at SD 12 in the center of the Lau Basin (> 100 km downstream the Tonga arc) **(c)** and the turbulent departure trajectory of the drifters released at LD 5-T5 and LD 5-T1 in the vicinity of the Tonga arc **(d)** can be appreciated. Drift velocities in the Lau Basin could be estimated from these trajectories by

following the evolution of the drifters' position over a given time period. Thus, a southwest drift velocity in the surface layer (0-15 m) was estimated at ~11 km d^{-1}.

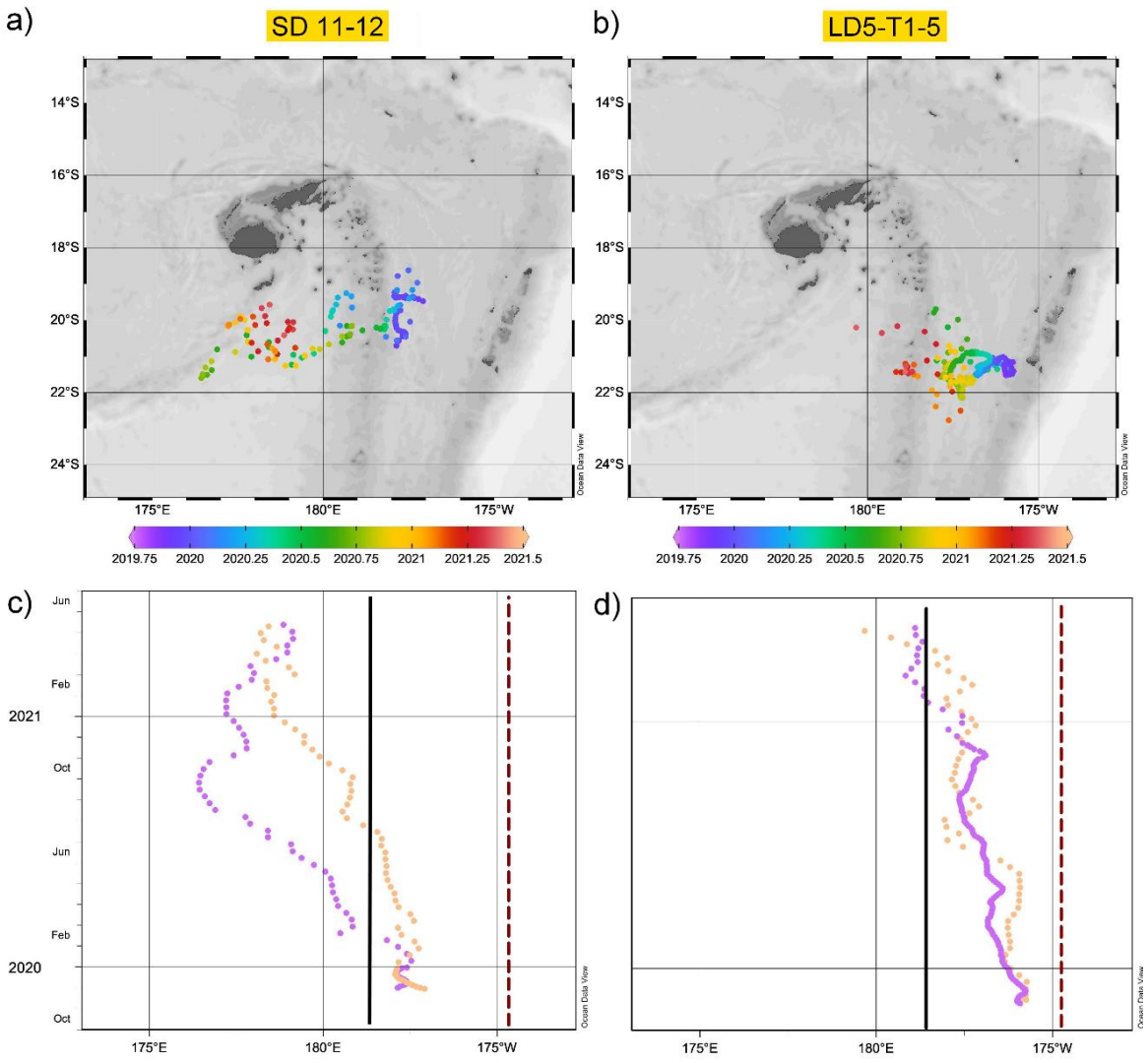

Figure S8. Trajectories of Argo floats released during the cruise at SD 11 and SD 12 **(a, c)** and at LD 5-T1 and LD 5-T5 **(b, d)**. The two maps represent the 1000 m-depth trajectories of the floats released at SD 11 and SD 12 **(a)** and at LD 5-T1 and LD 5-T5 **(b)** as a function of time. The graphs represent the unique trajectories as a function of time of each Argo released at SD 11 and SD 12 **(c)** and at LD 5-T1 and LD 5-T5 **(d)**, with each color corresponding to the trajectory of one float. The black line represents the Lau arc, the red dotted line represents the Tonga arc and the space between the two lines represents the Lau Basin. Note the predominantly southwestward trajectory of all floats in the Lau basin but drifting south or north along the Lau arc until finding deep sills to exit. Drift velocities in the Lau Basin could be estimated from these trajectories by following the evolution of the drifters' position over a given time period. Thus, a southwest drift velocity in the deep layer (1000-1500 m) was estimated at ~2 km d^{-1}.

Table S1. Validation of the dissolved iron (dFe) measurements by Flow Injection Analysis and Chemiluminescence detection (FIA-CL). This table summarizes the detection limits and total analytical blanks (pmol L^{-1}) of the apparatus, the standard measurements (nmol L^{-1}), and the different replicates performed.

See the separate Excel file entitled "Table S1".

		Mean values	Number of measures
Apparatus Validation	Detection limit (pmol L^{-1})	15.6 ± 6.73	n = 19
	Total analytical blank (pmol L^{-1})	21.6 ± 22	n = 19
Standard Validation	Standard GS measurement (nmol L^{-1})	0.519 ± 0.046 **Target**: 0.546 ± 0.041	n = 24
	Internal standard measurement (nmol L^{-1})	0.408 ± 0.041 **Target**: 0.386 ± 0.031	n = 33
Analysis Reproducibility	Standard deviation of analytical replicates (nmol L^{-1})	0 - 0.041	n = 12
Sampling Reproducibility	Standard deviation of samples from the same Go-Flo (nmol L^{-1})	0.002 - 0.025	n = 6
	Standard deviation of samples from different Go-Flo (nmol L^{-1})	0.008 - 0.166	n = 12

Note. Different replicates were measured to ensure the accuracy and reproducibility of the method. Replicates of the dosage system were performed by repeated analyses of the same sample several days apart. Replicates of the sampling protocol were performed in two ways: duplicates collected (1) from the same Go-Flo bottle and (2) from two different Go-Flo bottles closed at the same depth.

Table S2. Description of each sub-transect and statistical results of the Lagrangian Particle Tracking Experiment (LPTE).

See the separate Excel file entitled "Table S2".

Sub-transect →	**Melanesian waters**	**Lau basin**	**South Pacific gyre**
	19-21 °S, 175 °E-179 °W	19-21 °S, 179-174.5 °W	19-21 °S, 174.4-165 °W
End-member layer ↓	SD 2 and 3	SD 4, 11 and 12, LD 5 and 10	SD 6, 7 and 8
STUW	3.0 Sv (27%)	2.3 Sv (26%)	3.8 Sv (17%)
0-258 m 258 m thickness	average depth: 114 m	average depth: 110 m	average depth: 112 m
WSPCW	3.9 Sv (35%)	3.1 Sv (36%)	4.4 Sv (20%)
258-536 m 278 m thickness	average depth: 396 m	average depth: 398 m	average depth: 401 m
AAIW	3.7 Sv (33%)	3.08 Sv (36%)	4.6 Sv (21%)
536-1583 m 1047 m thickness	average depth: 999 m	average depth: 949 m	average depth: 1030 m
PDW	0.5 Sv (5%)	0.2 Sv (2%)	1.9 Sv (9%)
1583-3418 m 1835 m thickness	average depth: 2217 m	average depth: 1917 m	average depth: 2504 m
LCDW	0.01 Sv (0%)	-	7.2 Sv (33%)
>3418 m	average depth: 3577 m	-	average depth: 4400 m
Total Sv per sub-transect	11.1 Sv (27%)	8.7 Sv (21%)	21.9 Sv (52%)
Total Sv		41.7 Sv	

Note. This table shows the statistics of the quantitative results obtained for the LPTE performed in the three distinct sub-transects: Melanesian waters (western part), Lau Basin (central part) and South Pacific gyre (eastern part). Particle transport for each sub-transect is reported in Sverdrup (Sv). Average particle circulation depth is reported for each sub-transect and water mass. Percentages represent the proportion of particles reaching each water mass at each sub-transect relative to the initial total number of particles.

Table S3. Dissolved and particulate iron dataset along the cruise transect.

See the separate Excel file entitled "Table S3"

Note. Particulate iron data were used only to estimate the scavenging process in the 3-box budget for LD 5-T5 (sub-boxes 1 and 2 of box 1).

References

Arakawa, A., & Lamb, V. R. (1977). Computational Design of the Basic Dynamical Processes of the UCLA General Circulation Model. In *Methods in Computational Physics : Advances in Research and Applications* (Vol. 17, p. 173-265). Elsevier. https://doi.org/10.1016/B978-0-12-460817-7.50009-4

Artigue, L., Lacan, F., van Gennip, S., Lohan, M. C., Wyatt, N. J., Woodward, E. M. S., Mahaffey, C., Hopkins, J., & Drillet, Y. (2020). Water mass analysis along 22 °N in the subtropical North Atlantic for the JC150 cruise (GEOTRACES,

GApr08). *Deep Sea Research Part I: Oceanographic Research Papers*, *158*, 103230. https://doi.org/10.1016/j.dsr.2020.103230

Barnier, B., Madec, G., Penduff, T., Molines, J.-M., Treguier, A.-M., Le Sommer, J., Beckmann, A., Biastoch, A., Böning, C., Dengg, J., Derval, C., Durand, E., Gulev, S., Remy, E., Talandier, C., Theetten, S., Maltrud, M., McClean, J., & De Cuevas, B. (2006). Impact of partial steps and momentum advection schemes in a global ocean circulation model at eddy-permitting resolution. *Ocean Dynamics*, *56*(5-6), 543-567. https://doi.org/10.1007/s10236-006-0082-1

Blanke, B., Ahran, M., Madec, G., & Roche, S. (1999). Warm water paths in the equatorial Atlantic as diagnosed with a general circulation model. *Journal of Physical Oceanography*, *29*, 2753-2768.

Blanke, B., & Raynaud, S. (1997). Kinematics of the Pacific Equatorial Undercurrent: An Eulerian and Lagrangian Approach from GCM Results. *Journal of Physical Oceanography*, *27*, 1038-1053.

Gurvan, M., Bourdallé-Badie, R., Chanut, J., Clementi, E., Coward, A., Ethé, C., Iovino, D., Lea, D., Lévy, C., Lovato, T., Martin, N., Masson, S., Mocavero, S., Rousset, C., Storkey, D., Vancoppenolle, M., Müeller, S., Nurser, G., Bell, M., & Samson, G. (2019). *NEMO ocean engine*. https://doi.org/10.5281/ZENODO.3878122

Lettmann, K. A., Riedinger, N., Ramlau, R., Knab, N., Böttcher, M. E., Khalili, A., Wolff, J.-O., & Jørgensen, B. B. (2012). Estimation of biogeochemical rates from concentration profiles: A novel inverse method. *Estuarine, Coastal and Shelf Science*, *100*, 26-37. https://doi.org/10.1016/j.ecss.2011.01.012

Planquette, H., & Sherrell, R. M. (2012). Sampling for particulate trace element determination using water sampling bottles: Methodology and comparison to in situ pumps: Particulate trace element sampling. *Limnology and Oceanography: Methods*, *10*(5), 367-388. https://doi.org/10.4319/lom.2012.10.367